Aetheras: Characterising exoplanetary atmospheric escape with NIR and UV spectroscopy

Marius Anger, Aksel Søren Beltoft, Federico Biassoni, Johanna Noria Brecher, Antoine Corne, Jo Ann Egger, Simone Filomeno, Margarida Graça, Viktoria Keusch, Guillem Khairy, et al.

Acta Astronautica 238 (2026) 300–319

Contents lists available at ScienceDirect

Acta Astronautica

journal homepage: www.elsevier.com/locate/actaastro

Research paper

Aetheras: Characterising exoplanetary atmospheric escape with NIR and UV spectroscopy

Marius Anger [a,*], Aksel Søren Beltoft [b], Federico Biassoni [c,d], Johanna Noria Brecher [e], Antoine Corne [f,g], Jo Ann Egger [h], Simone Filomeno [i,j,k], Margarida Graça [l,x], Viktoria Keusch [m,n], Guillem Khairy [o], Jakub Kowalczyk [p], Riccardo Lasagni Manghi [q], Dominik F. Loidolt [r], Maja Marminge [s], Alex McDougall-Page [t], Lukas Tamulevicius [u], Elena Tonucci [v,w,x], Elise Wright Knutsen [y]

[a] Department of Electronics and Nanoengineering, Aalto University, Maarintie 8, Espoo, 02150, Finland
[b] DTU Space, Department of Space Research and Technology, Technical University of Denmark, Elektrovej Bygning 327, Kongens Lyngby, 2800, Denmark
[c] Como Lake Center for Astrophysics (CLAP), DiSAT, Università degli Studi dell'Insubria, Via Valleggio 11, Como, 22100, Italy
[d] INAF – Osservatorio Astronomico di Brera, Via E. Bianchi 46, Merate, 23807, Italy
[e] Institut für Geophysik und Extraterrestrische Physik, TU Braunschweig, Mendelssohnstraße 3, Braunschweig, 38106, Germany
[f] Department of Earth Sciences, Palaeobiology, Uppsala University, Villavägen 16, Uppsala, 75236, Sweden
[g] Department of Earth Sciences, University of Lille, Cité Scientifique, SN5, Villeneuve d'Ascq, 59650, France
[h] Weltraumforschung und Planetologie, Physikalisches Institut, Universität Bern, Gesellschaftsstrasse 6, Bern, 3012, Switzerland
[i] INAF-Osservatorio Astronomico di Roma, Via Frascati 33, Monte Porzio Catone (RM), I-00040, Italy
[j] Dipartimento di Fisica, Università di Roma Tor Vergata, Via della Ricerca Scientifica 1, Roma, I-00133, Italy
[k] Dipartimento di Fisica, Sapienza Università di Roma, Piazzale Aldo Moro 5, Roma, I-00185, Italy
[l] Faculdade de Ciências da Universidade de Lisboa, Campo Grande 016, Lisbon, 1749-016, Portugal
[m] Institute of Theoretical Physics - Computational Physics, Graz University of Technology, Petersgasse 16, Graz, A-8010, Austria
[n] Institute of Physics, University of Graz, Universitätsplatz 5, Graz, A-8010, Austria
[o] Faculty of Science, Technology and Medicine, University of Luxembourg, Bâtiment L 6, rue Coudenhove-Kalergi, L-1359, Luxembourg
[p] Warsaw University of Technology, pl. Politechniki 1, Warsaw, 00-665, Poland
[q] Università di Bologna, Department of Industrial Engineering, Via Fontanelle 40, Forlì, I-47121, Italy
[r] Department of Astrophysics, University of Vienna, Türkenschanzstraße 17, Vienna, 1180, Austria
[s] Uppsala University, Lägerhyddsvägen 1, Uppsala, 75237, Sweden
[t] Mechanical and Aerospace Engineering, University of Strathclyde, 16 Richmond St, Glasgow, G1 1XQ, Scotland, UK
[u] Vilnius Gediminas Technical University, Saulėtekio al. 11, Vilnius, LT-10223, Lithuania
[v] Delft University of Technology, Faculty of Aerospace Engineering, Kluyverweg 1, Delft, 2629 HS, Netherlands
[w] Netherlands Institute for Space Research (SRON), Niels Bohrweg 4, Leiden, 2333 CA, Netherlands
[x] Leiden Observatory, Leiden University, PO Box 9513, Leiden, 2300 RA, Netherlands
[y] LATMOS/IPSL, UVSQ Université Paris-Saclay, Sorbonne Université, CNRS, 11, boulevard D'Alembert, Guyancourt, 78280, France

ARTICLE INFO

Keywords:
Exoplanets
Atmospheric escape mechanisms
Magnetic fields
Radius valley
Hot Neptune desert
Spacecraft design

ABSTRACT

To date, many exoplanets have been discovered which exhibit distinct characteristics not observed within our own Solar System, raising numerous unresolved questions regarding their compositions, atmospheres, formation processes, and evolutionary pathways.

Several missions have been dedicated to enhance the understanding of the exoplanets like James Webb and Hubble Space Telescopes. However, they have a limited spectral range and resolution to allow for a complete characterisation of atmospheric dynamics. The Aetheras mission proposal was developed at the Summer School Alpbach 2023 and presents a satellite mission to overcome these limitations to better understand the formation, evolution and characteristics of exoplanets. This mission aims to unravel key enigmas in contemporary

* Corresponding author.
E-mail addresses: marius.anger@aalto.fi (M. Anger), federico.biassoni@inaf.it (F. Biassoni), j.brecher@tu-braunschweig.de (J.N. Brecher), jo-ann.egger@unibe.ch (J.A. Egger), simone.filomeno@inaf.it (S. Filomeno), vkeusch@student.tugraz.at (V. Keusch), riccardo.lasagni@unibo.it (R.L. Manghi), dominik.loidolt@univie.ac.at (D.F. Loidolt), alex.mcdougall-page.2020@uni.strath.ac.uk (A. McDougall-Page), e.w.knutsen@its.uio.no (E.W. Knutsen).

https://doi.org/10.1016/j.actaastro.2025.08.042
Received 6 November 2024; Received in revised form 23 May 2025; Accepted 22 August 2025
Available online 11 September 2025

exoplanetary research by investigating atmospheric escape mechanisms and measuring proxies of magnetic fields' influence on atmospheric loss. Focusing on objects in the Radius Valley and the Hot Neptune desert, the mission seeks to discover their origins.

By defining mission needs and designing a potential instrument based on derived requirements, a space mission architecture is envisioned to fulfil the proposed mission objectives. A spacecraft design has been made with top down systems engineering approach.

Employing transit spectroscopy in the near-infrared range (1070 nm to 1090 nm) and ultraviolet range (115 nm to 285 nm) outside the geocoronal influence, the mission gains valuable insights to planetary formation and evolution. The mission architecture comprises a 1302 kg spacecraft equipped with a 1.5 m main mirror to observe the sky over a mission lifetime of three years.

1. Introduction

As of April 2024, the ever expanding exoplanetary catalogue comprises over 5000 confirmed celestial bodies, each distinguished by a distinctive array of characteristics. These properties may include radius, mass, core composition, atmospheric makeup (if applicable), proximity to the host star, and orbital period, as documented by the Exoplanet Archive [1]. This vast and diverse collection underscores the complexity of exoplanetary systems and raises questions about the formation and evolution of planetary systems. The underlying patterns and mechanisms governing these distant worlds are still not fully understood, raising the need for further exploration and investigation.

The number of detected exoplanets is already high enough to allow for statistically significant demographic analysis. Notably, with respect to planetary mass, orbital period, and radius, four distinct categories emerge as illustrated in Fig. 1:

- **Brown Dwarfs**: Brown Dwarfs are astrophysical bodies massive enough to fuse deuterium but not enough to fuse hydrogen (approximately $10 < M < 80$ Jupiter masses) [2],
- **Hot Jupiters**: Gas giant exoplanets with an orbital period of less than 10 days and located closer than 0.1 AU from their host star [2],
- **Sub-Neptunes**: Planets with a smaller radius than Neptune but near $2.0\,R_E$ (Earth radii) [3],
- **Super-Earths**: Planets with a larger radius than Earth, yet lighter than ice giants [3].

Hot Jupiters and Brown Dwarfs possess magnetic fields. One explanation of the origin of these magnetic fields is their fast rotation period, but this phenomenon is not yet fully characterised [4–6]. Besides, observations support the theory that atmospheric escape is taking place on Brown Dwarfs [7–9]. However, it is still debatable whether an intrinsic magnetic field enhances or prevents atmospheric escape [10]. Even though studies have already been conducted to understand the atmospheric properties of these distant objects, better quality data would enable statistically significant analysis [11,12].

Additionally, one can note the scarcity of the Brown Dwarf companions in close orbits around solar-type stars. The Brown Dwarf desert describes the phenomenon that more brown dwarfs have been found freely floating than bound to a system [13,14]. The current hypothesis includes Brown Dwarfs merging with their host stars or interacting with other companions during the evolution of the protoplanetary disk, or Brown Dwarfs forming at larger distances [15–18].

Another conspicuous void is evident in the planetary count within the region indicated in green in Fig. 1. Referred to as the "Hot Neptune desert", this region is characterised by a scarcity of Neptune-sized planets orbiting in close proximity to their host stars [19]. The notable absence in this less densely populated zone cannot be attributed to any discernible observational bias, thereby implying the influence of underlying processes [20]. Close-in gaseous planets are believed to lose their atmospheres due to intense stellar irradiation, which may explain the scarcity of hot Neptunes. This atmospheric loss could result from hydrodynamic escape, with some planets being completely stripped or retaining their envelopes depending on their initial mass, and may also suggest different formation and evolution mechanisms or high-eccentricity migration [19,21].

Comparably to the Hot Neptune desert, a distinct gap is discernible in the number of planets per star, specifically within the radius range of $1.5\,R_E$ to $2.0\,R_E$, as illustrated in Fig. 2. This phenomenon is known as the "Radius Valley".

The causes of the Radius Valley and the Hot Neptune Desert are still actively debated. One hypothesis claims that the Radius Valley represents an unstable region where planets transition towards a stable radius. This transformative process is believed to be initiated by mechanisms such as atmospheric escape, including phenomena like photoevaporation [23]. This process, in which high energy radiation removes the exoplanetary atmosphere, could lead to envelope-powered mass loss by disabling the atmosphere of the exoplanet from retaining core heat [21,24]. While these processes are key contenders, alternative hypotheses are proposed, encompassing various factors [25,26]. For example, a recent theory is the water-rich Sub-Neptune hypothesis [24, 27–29]. This hypothesis originates from identifying wide variance in densities within the known radius valley exoplanets that cannot be accounted for assuming only rock or gas densities. Instead, it is theorised that these planets may have large quantities of water present in various forms from thick ice layers to supercritical vapour [30–34].

Numerous planetary features potentially influence the radius transition. The presence or absence of an intrinsic magnetic field is one of the noteworthy candidates [35]. Despite the ongoing challenge of unambiguously detecting exoplanetary magnetospheres due to, for example, weak radio signals and as magnetic fields are usually measured in situ, the topic is being actively explored [36–39]. Recent developments [35] challenge the conventional hypotheses that a planetary magnetic field solely aids in retaining atmospheres by deflecting ionising stellar wind, but can rather have additional influence on the atmosphere and the planet's surface temperature [40–42]. On the other hand, the presence of a magnetic field has been claimed to amplify the interaction area with the solar wind, resulting in stronger magnetic reconnection events and subsequent enhancement of ion up flow and cold plasma outflow [43]. These factors show the complexity of planetary evolution and atmospheric dynamics.

The Aetheras mission concept, as outlined in this paper, was started at the Summer School Alpbach 2023 and analyses the requirements for enhancing our understanding of exoplanets in the Radius Valley and the Hot Neptune desert. The proposed mission design involves a spacecraft at the Earth–Sun system's L2 point, utilising spectroscopy to investigate the atmospheric tails of exoplanets.

2. Science questions and objectives

The overarching scientific theme of Aetheras is:

Deepening our understanding of planetary system formation and evolution through the study of atmospheric escape.

In alignment with this mission statement, Aetheras seeks to address the following scientific objectives:

SO1. Are there correlations between the characteristics of exoplanets, the properties of their host stars, and the occurrence of atmospheric escape?

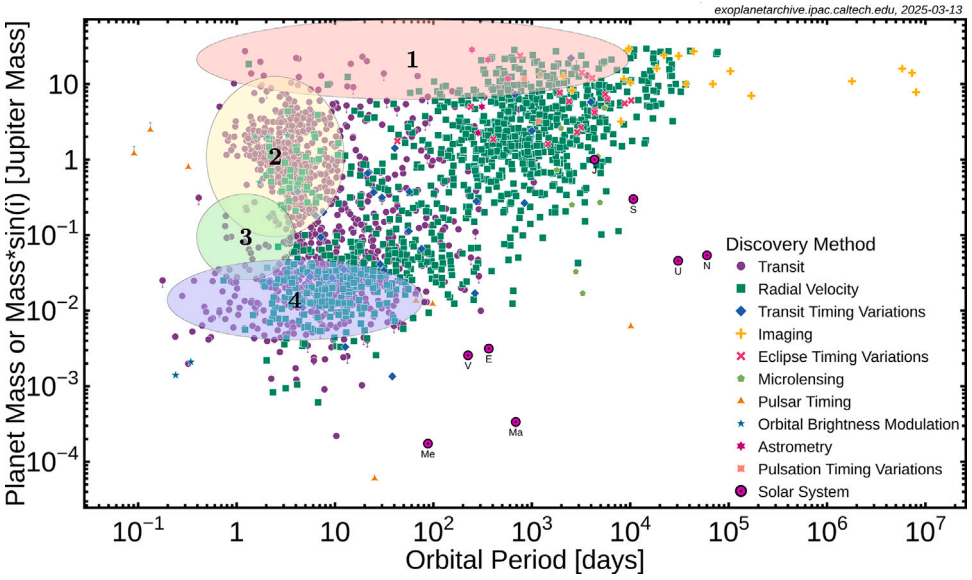

Fig. 1. Distribution of discovered exoplanets according to their orbital period and mass. The red ellipse (1) and yellow ellipse (2) mark the regions of Brown Dwarfs and Hot Jupiters respectively. The green circle (3) indicates the Hot Neptune dessert. The blue ellipse (4) on the bottom represents the area of Super-Earths and Sub-Neptunes. The image was generated by the NASA Exoplanet Archive [1].

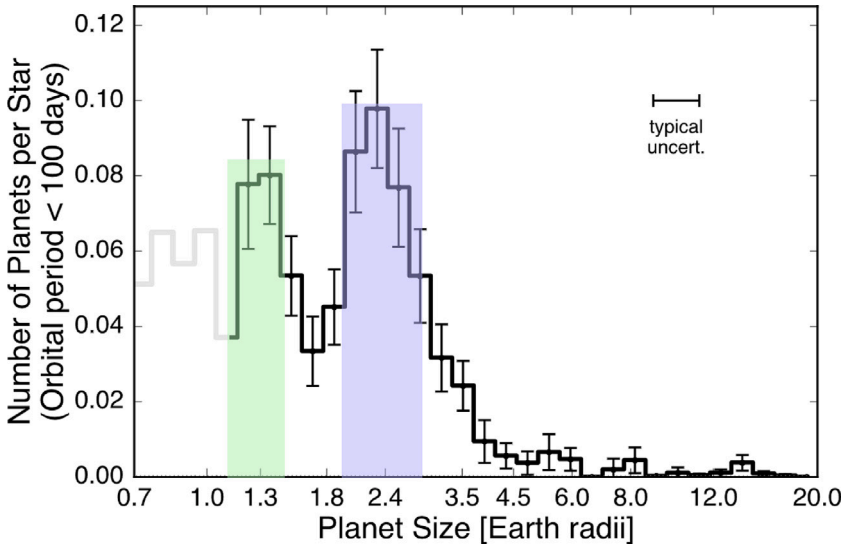

Fig. 2. Number of planets per star according to their orbital period. Highlighted in green (left) and blue (right) are the distributions of Super-Earths and Sub-Neptunes respectively. In between lies the so-called Radius Valley.
Source: Adapted from Fulton et al. [22]. ©AAS. Reproduced with permission.

SO2. Is atmospheric escape a factor in creating the observed Radius Valley in exoplanetary systems?
SO3. Is atmospheric escape a factor in creating the Hot Neptune Desert, a phenomenon observed in certain regions of the mass-orbital period space?
SO4. How does the magnetic field of exoplanets influence atmospheric escape, and does the presence or absence of a magnetic field affect the rate and nature of atmospheric loss?

3. Detection methods

To answer these questions, the mission will characterise the atmospheric escape processes and the magnetic fields of transiting exoplanets. Currently, only indirect methods are available to observe these phenomena.

3.1. Atmospheric escape detection

Atmospheric escape can be studied through transmission spectroscopy conducted during the transit of a planet. A planetary exosphere escaping from the planet has the potential to extend over several planetary radii, manifesting as a comet-like tail. Three-dimensional simulations as seen in Ehrenreich et al. [44] or Khodachenko et al. [45] illustrate such a tail coplanar with the line of sight. It releases hydrogen atoms isotropically from the Roche lobe limit of an exoplanet, to create a tail. The presence of the tail influences the absorption of starlight during the planetary transit, which can be seen in light curve spectroscopy [46]. This in-transit excess absorption caused by the tail can indicate an escaping exosphere [47].

Typically, the transit depth exhibits variations ranging from less than 1 % up to 56 % in specific absorption lines for a Neptune-mass planet [44], signifying the presence of an outflow. The transit duration

can give a direct measurement of exoplanets' atmospheric outflow velocity [48].

The primary indicators of atmospheric escape are observed in distinct spectral lines, notably the hydrogen Ly-α line (121.6 nm), the He I triplet metastable state transition line (1083 nm), and heavier species such as C II (133.45 nm). Hydrodynamic mechanisms describe the atmospheric escape of these species within the exospheres [49].

Observations of the Ly-α involve time-series observations of the Ly-α line of the host star before, during, and after the planetary transit, as illustrated in Fig. 1 in Ehrenreich et al. [44]. However, due to significant absorption by the interstellar medium (ISM), the Ly-α line is most effectively studied by observing its wings, where the flux is less attenuated [50]. Due to the high systemic velocities of some targets, the core of the Ly-α line may be shifted and hence not entirely absorbed by the ISM. However, given the low resolution of the instrument, the line will appear as a broad feature rather than being fully resolved (e.g., see Fig. 3(b)). As a result, Aetheras is still sensitive to flux variations over large spectral bins, and it is able to detect Ly-α changes independently of Doppler shifts or ISM absorption.

Interactions with the exosphere, particularly with the tail, often result in asymmetries compared to a traditional transit light curve at longer wavelengths.

A characteristic exospheric signal includes a decrease in flux within the stellar Ly-α line during a planetary transit, often accompanied by an extended egress and pre-transit absorption. This flux reduction is particularly prominent in the blue-shifted wing due to the outflow direction, as described in Ehrenreich et al. [44]. A key advantage of low-resolution spectrographs mounted on space-borne facilities is their larger wavelength bins, which collect more flux per bin, significantly increasing the SNR compared to high-resolution spectrographs on the ground. Such characteristic allows for a clearer detection of Ly-α variations between before, during, and after transit phases. This enables a synergy between high-resolution ground-based observatories and low-resolution space borne telescopes, where the former provides detailed kinematic and compositional insights, while the latter offers robust detection of broad spectral variations.

Similar to the Ly-α line, the He I triplet can be used to estimate atmospheric escape rates and to study planetary outflows [51]. By observing the He I line spectrum during the transit, one can witness changes in absorption attributed to the excess absorption caused by helium atoms escaping the planetary atmosphere, akin to the observations made for Ly-α (refer to Fig. 3 in Zhang et al. [23]).

The information derived from the He I line complements that obtained from the extended wings of the Ly-α line, as the absorption process occurs in different sections of the atmospheric tail. Therefore, one can probe a different region of the outflow and simultaneous He I line observations aid in constraining theoretical models of escaping exoplanet atmospheres [51]. However, the He I triplet absorption is highly dependent on the stellar Extreme Ultra-Violet (XUV) flux, a parameter largely unknown for most observed stars due to the scarcity of observations in this wavelength range. Additionally, there is a strong degeneracy between stellar XUV flux and the He/H number density ratio in the planet's atmosphere. Potential detections of the He I triplet, combined with simultaneous observations of Ly-α or Hα, can provide a more precise estimate of the stellar XUV flux and the He/H abundance in the planetary atmosphere when compared with simulations. Using the ATmospheric EScape code (ATES) [52] and the Transmission Probability Module (TPM) [53], it is possible to self-consistently model both a planet's mass-loss rate and the absorption profiles of Ly-α, Hα, and He I triplet. Space-based observations, free from telluric contamination, combined with theoretical modelling, will enable tighter constraints on the stellar XUV flux and the planetary He/H ratio. ATES and TPM codes are used to simulate the exoplanet HAT-P-32b, a well-known target, and despite the reduction of the line depth, it is possible to detect these lines even at low resolution. The simulated observations are seen in Fig. 3(a).

The transit spectroscopy technique employed in Ly-α and He I studies can be extended to metals, offering the advantage of significantly reduced or absent interstellar medium (ISM) absorption [49].

These include *N* I at 119.9 nm, Si I at 124 nm, H_2O at 128 nm, O I at 130.4 nm, C II at 133.4 nm, Si III at 150 nm, C III at 155 nm, Al I at 169 nm, and Na II at 280.9 nm. These metal lines are notably weaker and narrower compared to Ly-α, posing limitations on the precision with which transit depths and outflow velocities can be measured. Due to these constraints, the focus of extensive research has been on the most intense line of C II (133.4 nm). The advantage of exploring various spectral lines, ranging from light elements such as H and He I to heavier metals like C II, lies in the enhanced understanding of atmospheric escaping processes in addition to the resilience against effects like the interstellar medium. Additionally, one can extract information about the host star and the atmospheric composition. Some of these lines, such as the He I and the Hα, have also been observed with ground-based telescopes together with spectrographs (e.g. [54–56]) and also used to investigate atmospheric escape, for example by Paragas et al. [57] utilising a telescope of the Palomar Observatory. However, a major advantage of using space-borne instruments to observe these lines is the ability to target much fainter objects, which would be challenging with ground-based high-resolution instruments. This limitation arises because, at low resolution, the larger wavelength bin collects more light, resulting in a higher SNR, making the detection of these lines feasible. Additionally, space-based observations eliminate the issue of telluric contamination. In particular, near the He I triplet, OH emission lines can overlap with He I absorption, depending on the Barycentric Earth Radial Velocity (BERV) and the system's systemic velocity. This imposes stringent observational constraints for ground-based detection of He I lines, further underscoring the advantage of space-based instrumentation.

Despite the low resolution, Hα can still be a valuable observable. This is because the small number of spectral bins and the high sensitivity to flux allow for precise photometric measurements. Rather than attempting to analyse this line through traditional transmission spectroscopy, this mission focuses on photometric observations, as the setup is particularly sensitive to flux variations. Consequently, this approach enables the tracking of flux changes as a function of orbital phase.

3.2. Magnetic fields and bow shock detection

In addition to characterising the atmospheric escape, ionised metal species can be sensitive to planetary magnetic fields, forming controlled outflows and producing asymmetric transits if the field is strong enough [58]. For this process, the C II line is the most used line studied by observing flux variation and asymmetries during planetary transit (e.g. [59,60]).

Another phenomenon that can be used as a proxy for the presence of a magnetic field is the bow shock [61,62], which occurs when the stellar wind interacts with the magnetosphere of a planet, due to a sudden decrease in the speed of the stellar wind particles. If the relative motion between the objects and stellar coronal material is supersonic, then the bow shock forms in the direction of motion. When the shocked material's optical depth is high enough, starlight is absorbed, and produces an early ingress in the transit light curve, as seen in Fig. 4.

Even if transit asymmetries for escaping metals are a matter of debate in the literature [64–66], early results pointed out the presence of a magnetospheric bow shock around WASP-12 b [63], while others have not found any evidence [67]. Additional observations ruled out a stable early ingress [68], and the possibility of a variable bow shock remains open [49].

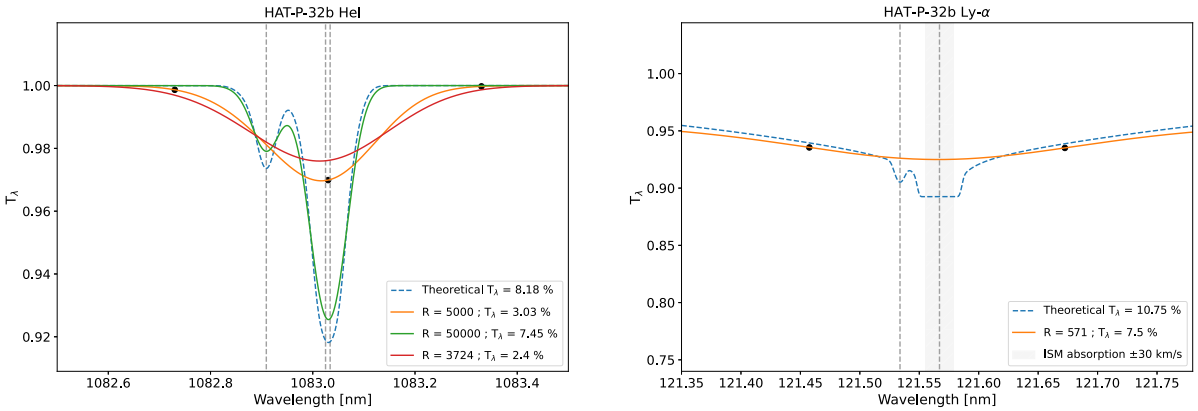

(a) HAT-P-32b HeI triplet simulations obtained with ATES and TPM [34, 26]. The dashed blue line represents the theoretical absorption profile of the HeI triplet with infinite resolving power. The green line represents the profile obtained with a high-resolution instrument such as GIANO-B, while the orange one is the predicted absorption profile with R=3724. The black dots are the positions of Aetheras bins, while the grey dashed lines are the theoretical positions of HeI absorption lines.

(b) HAT-P-32b Ly-α simulations obtained with ATES and TPM [34, 26]. The grey vertical region represents the ISM absorption. The two dashed grey vertical lines correspond to the theoretical Ly-α centred at 121.567 nm, and the Deuterium line at 121.534 nm Wavelengths shown in a vacuum.

Fig. 3. Absorption line simulation of HAT-P-32b for HeI triplet (a) and Ly-α (b) measured with different resolutions.

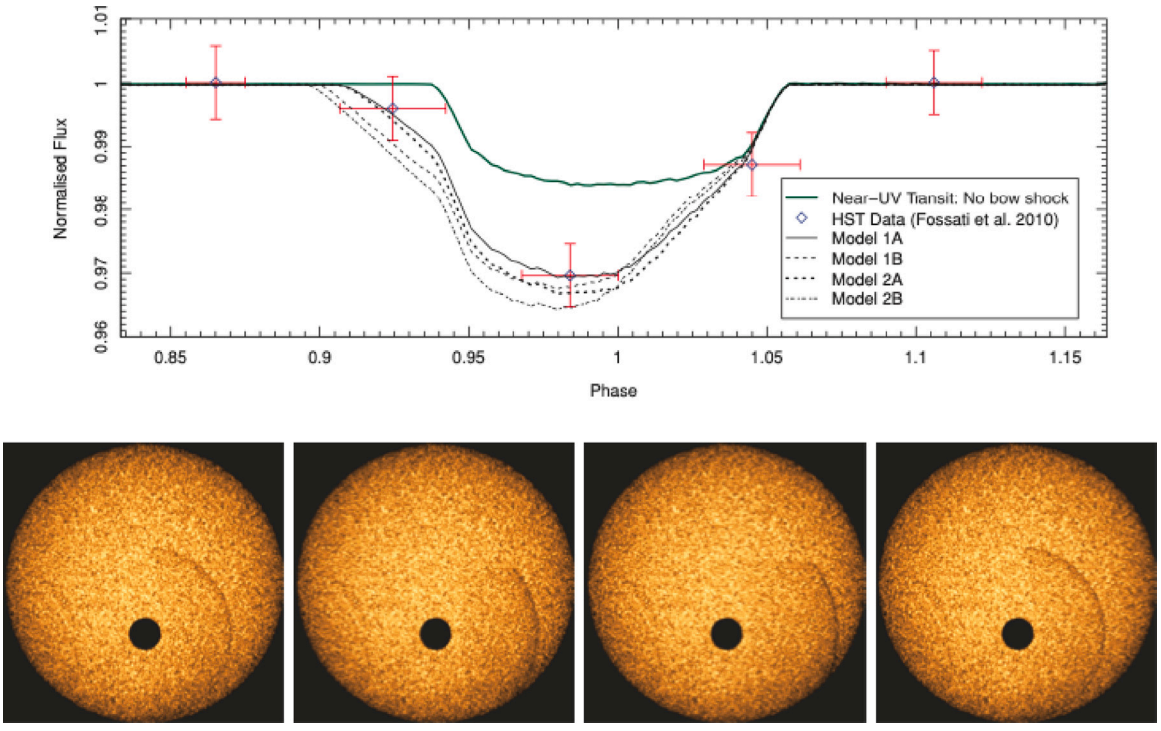

Fig. 4. Top panel: Modelled transits around WASP-12 b in the near-UV, considering scenarios with and without a bow shock (green and black, respectively). The Hubble Space Telescope (HST) observations are represented in red, while the black lines depict simulation results. Bottom panel: Simulated mid-transit images. Figure 2 from Llama et al. [63]. Reproduced with permission by Oxford University Press.

4. Targets

Given the scarcity of detected exoplanets within the Radius Valley, a potential target list is compiled, encompassing various categories of planetary bodies that the mission aims to observe. This list includes both possible targets (where the existence of the body is uncertain) and targets with a probable certainty of existence. Additional targets in the Hot Jupiter and Brown Dwarf regions have been selected to study exoplanetary magnetospheres.

The selection of targets was guided by Aetheras' scientific objectives, considering factors such as distance from Earth, absolute magnitude, and orbital period. These criteria are cross-referenced with the NASA planetary archive [1].

The following criteria for target selection are considered:

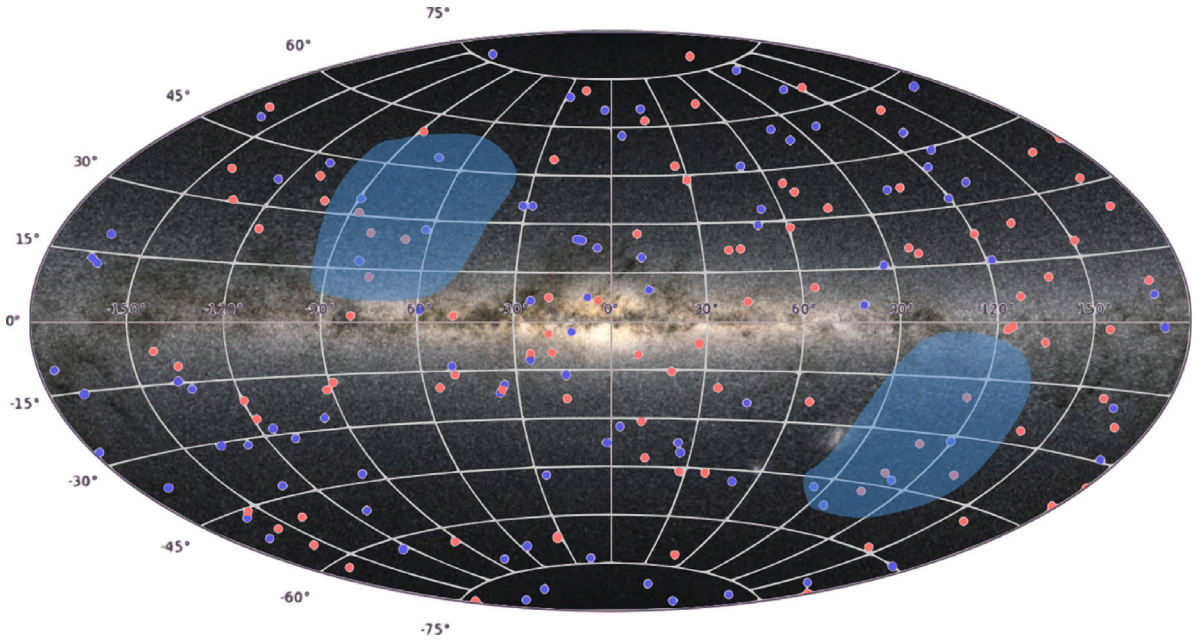

Fig. 5. Celestial sphere image in a Galactic coordinate reference system. Targeted exoplanets are marked with red dots (Radius Valley) and purple dots (Hot Neptunes, Hot Jupiters, Brown Dwarfs). Additionally, the two provisional long-duration fields proposed by the space telescope PLATO are indicated in blue [76].

- **Planets in the Radius Valley:** Planets with radii between 1.5−2.0 R_{Earth}, orbital periods less than 100 days, and located within a maximum distance of 40 parsec.
- **Planets Around the Radius Valley:** Planets with radii between 1.2 – 1.5 R_{Earth} and 2.0 – 2.3 R_{Earth}, orbital periods less than 100 days, and located within a maximum distance of 40 parsec.
- **Hot Jupiters:** Hot Jupiters with a maximum mass of 13.6 M_{Jup}, orbital periods of maximum 10 days, and located within a maximum distance of 200 parsec.
- **Brown Dwarfs:** Brown Dwarfs were manually selected from relevant papers (e.g. [69–75]).

120 exoplanets in and around the Radius Valley in the planetary archive fulfil the criteria at the time of writing along with 30 Brown Dwarfs, 100 Hot Jupiters, and 50 Hot Neptunes. A map of the target exoplanets' position on the projection of the celestial sphere is shown in Fig. 5. It becomes apparent that the targets are homogeneously distributed in the sky as they are all close to our solar system.

Furthermore, current and future missions are anticipated to confirm additional target exoplanets. Notably, the PLATO space telescope [77,78], scheduled for launch in 2026, is expected to identify an estimated 450 – 8000 Radius Valley targets and 6000 – 20000 Hot Jupiters [76]. These potential discoveries could be considered for addition to the target list to extend the mission.

5. Current and future missions

Several space observatories, including the Hubble Space Telescope (HST) [79,80], the James Webb Space Telescope (JWST) [81], and the future Atmospheric Remote-sensing Infrared Exoplanet Large-survey (Ariel) [82,83], can be utilised to characterise exoplanet atmospheres.

The JWST's Near-Infrared Spectrograph (NIRSpec) covers a wavelength range of 0.6 μm to 5.3 μm and can study the He I emission line [84]. However, as detailed in later sections, a comprehensive characterisation of Aetheras' targets would demand dedicated observation times of roughly 12000 hours, occupying a substantial portion of the already busy JWST observational schedule. Moreover, the absence of a UV spectrometer on the JWST constrains the scope and depth of findings compared to what could be achieved through a dedicated mission.

Scheduled for launch in 2029, the Ariel mission aims to conduct atmospheric characterisation of about 1000 transiting exoplanets using transit spectroscopy, spanning the wavelength range from 1.95 μm to 7.8 μm [85]. However, Ariel lacks a UV spectrometer capable of detecting the Ly-α line and other specific UV emission lines, indicating atmospheric loss or the presence of a magnetosphere. Additionally, the low resolution in the near-IR (R> 10) and mid-IR (R= 30 – 200) of the Ariel InfraRed Spectrometer (AIRS) does not resolve the He I line, limiting the ability to detect the rate of atmospheric escape.

Ly-α observations can only be obtained by the HST, equipped with UV instruments (Cosmic Origins Spectrograph (COS) / Space Telescope Imaging Spectrograph (STIS)). Complexities in the data interpretation may arise, such as interstellar absorption and Earth geocoronal emission contamination [37,86]. Additionally, HST observations are subject to limitations due to Earth occultations, restricting the precision of measurements [49]. The inherently limited sensitivity of the instruments may result in a significant number of planets remaining undetectable [48].

Besides, it is important to consider Aetheras in the context of ESA's Voyage 2050 program, specifically the mission statement "From temperate exoplanets to the Milky Way" [87–93]. In this context, Aetheras provides simultaneous spectroscopy in the NIR-VIS-UV spectrum. Missions such as NewAthena, Pandora or MAUVE, while also targeting atmospheric observations, can only in combination provide the same range and require coordination with each other to do simultaneous observations [94–97]. Furthermore, NASA's HWO also intends to provide observational capability in this range, underlining this demand. Although HWO will provide means for studying atmospheric escape, the authors believe that, much like JWST, it will not be possible to perform these observations for the vast number of targets already known due to the required observation times [98,99]. The Aetheras mission may be able to 'split the gap' between temperate exoplanets and the larger galactic ecosystem.

The Extremely Large Telescope, currently under construction, will play a significant role in characterising small exoplanets using high-resolution spectroscopy, providing crucial insights into atmospheric composition [100,101]. However, much like other ground-based facilities as discussed above, it will face limitations due to atmospheric interference and the availability of observation time, particularly for faint targets.

The proposed Aetheras space-based mission uniquely integrates UV and IR spectrometers to provide insights into the mechanisms of atmospheric evolution of exoplanets and shed light on the coevolution of their atmospheres and magnetospheres.

6. Science requirements

In order to address the scientific questions outlined in Section 2, the following science requirements [SR] shall be fulfilled:

SR1. The mission shall simultaneously measure proxies for atmospheric escape and magnetic fields in the Near-Infrared (NIR), Ultra-Violet (UV) and Visual (VIS), including the absorption lines [SO1, SO2, SO3, SO4]:

- H Ly-α (121.40 nm to 121.75 nm),
- C II (130.00 nm to 137.00 nm),
- Mg II (277.00 nm to 281.00 nm),
- Hα (655.00 nm to 657.00 nm) and
- He I (1082.60 nm to 1084.00 nm)

This requirement is derived from the previously explained measurement methods. In the investigation of planetary system formation through atmospheric escape mechanisms, the specified spectral lines serve as indicators of the escaped particle tail (H Ly-α, Mg II, He I, C II), as well as the presence of a magnetic bow shock (Mg II and C II).

In order to further study a possible correlation between an exoplanet's radius and its atmospheric properties, the mission will observe exoplanets from the following target groups:

SR2. The mission shall observe at least 100 transiting exoplanets that lie in the Radius Valley or on its edges ($1.2 < R < 2.3 R_E$) using spectroscopy. [SO1, SO2, SO4]

SR3. The mission shall observe at least 100 transiting objects with a mass of at least 0.1 Jupiter masses. [SO1, SO4]

SR4. The mission shall observe at least 25 transiting Neptune-sized exoplanets with orbital periods of less than 4 days. [SO1, SO3, SO4]

For each of these observations, the following requirement is established to ensure the comprehensive capture of the full transition of an exoplanet.

SR5. The mission shall observe a minimum of 4 full transits per target, including ingress and egress, with a 2 h margin before and 50% transit duration margin after, acquiring at least 40 equidistant measurements per transit. [SO1, SO2, SO3, SO4]

The observation of the host star prior to the transit is crucial for obtaining a reference spectrum for the subsequent transit. Moreover, considering that the bow shock is situated in front of the planet, its effects become measurable within the two-hour interval before the transit. Given that atmospheric escape is modelled as an outflow of particles, the measurement of this particle tail is conducted during and after the transit duration.

To identify the different spectral lines, the following resolutions in the respective bands are required:

SR6. The spectral resolution in the NIR shall be sufficient to measure a Doppler shift of at least $85\,\mathrm{km\,s^{-1}}$ in the He I absorption line. [SO1, SO2, SO3, SO4]

SR7. The spectral resolution in the UV shall be able to at least separate the Si III absorption line from the Ly-α absorption line. [SO1, SO2, SO3, SO4]

7. Instruments

With these science requirements, the following requirements for the needed instruments, as well as their design, can be derived.

7.1. Instrument requirements

To ensure that the Science Requirements are met, Instrument Requirements [IR] are defined as seen in Table 1. It becomes apparent that a single instruments is not able to resolve all needed spectra, as the two wavelength bands are too widely separated. Additionally, with the separation, optimisation for each wavelength band can be done, increasing the respective efficiency.

7.2. Optics

Using the requirements listed in Table 1, two separate spectrometers are envisioned to resolve the NIR and UV ranges. A fine guidance system is also necessary to ensure sufficient acquisition precision of the target stars.

The optical layout, starting from the main mirror, is seen in Fig. 6. The related parameters, such as mirror size and field of view, are shown in Table 2. This must only be considered a preliminary baseline, recognising that further development is required for the detailed optical path and the detector designs of the proposed setup.

The light is collected by a Cassegrain telescope with a narrow angular field of view of 3.14° and a diameter of 1.5 m [M1] to be able to detect the faintest star in the target list within the required time. The secondary mirror [M2] is integrated with a tip-tilt actuator to reduce the jitter of the point source on the detector at the end of the optical path, caused by the vibrations of the spacecraft service module. The visible (VIS) channel provides information on the Hα line while a fine guidance system channel (FGS) is required to provide a steering signal for the tip-tilt mirror [TTM/M2] for fine target acquisition. This channel is not discussed in detail as several systems have already been developed for this purpose, such as the Fine Guidance System for the HST [102–104].

A collimator [COLL1] brings the beam size down to 2 cm. The first dichroic mirror [DICH1] filters the UV light by spatial separation at a cut-off frequency of 300 nm to supply the UV instrument. The remaining frequencies are split into the VIS/FGS channel and the NIR channel by a second dichroic mirror [DICH2] with a cut-off frequency of 950 nm.

In each spectrometer, a focusing mirror [UV-M1, NIR-M1] is used to adjust the focal stop of the main mirror ($f/24.4$) to the needed focal stop of the respective instrument. The focusing mirrors are also used to focus the light through a slit [UV-SLIT, NIR-SLIT]. This is needed to restrict the light beam to the selected target star onto a concave blazed holographic diffraction grating [UV-GRAT, NIR-GRAT], which allows a shorter optical path and fewer optical elements, thus increasing the throughput of the system. A grating strata number of 100 results in a smooth response across the UV range and can yield an average grating efficiency of 68 % [105,106]. Several grating technologies have already been developed for NIR instruments and could be reused here to achieve reflectances around 88 % at 1000 nm [106,107]. At the focus of the diffraction grating, a CCD [UV-DET, NIR-DET] is used to count the collected photons.

The light from DICH2 is further split into the FGS and VIS channel by another dichroic mirror [DICH3]. The respective focusing lenses for each channel [VIS-M1, VIS-M2] confine the light beam onto the VIS detector and the target acquisition instrument respectively.

A high reflectance coating, especially for surfaces reflecting UV light, must be employed as fewer photons in this spectrum are emitted than in NIR. Protected Aluminium mirrors have been chosen for this as they can be manufactured quickly and have a high reflectance value of around 70 % at 120 nm [108]. This material can also reflect NIR up to 90 %. The presented optical system (Fig. 6) allows a maximum throughput of 13.22 % in the UV and 34.70 % in the NIR channel before splitting it into spectral bins as seen in Table 3.

7.3. UV detector considerations

For UV detection, several detector types can be considered [109]. Recent studies have shown that GaN-based photocathodes in reflection mode exhibit great potential for efficient detectors down to 110 nm at room temperatures [110,111]. These detectors, known as electron bombardment CCDs (EBCCDs), are paired with a photocathode in close proximity, resulting in a combined quantum efficiency of up to 45 % at 120 nm [112,113].

Assuming a pixel size of 13 µm, a minimum of 1143 pixels is required to cover the spectral range of 115 nm to 285 nm, resulting in a spectral

Table 1
Instrument Requirements [IR].

IR1.	The spacecraft shall be equipped with a spectrometer to perform simultaneous observations in the NIR $(1082.60 - 1084.00) \pm 0.05$ nm and UV $(121.40 - 281.00) \pm 0.05$ nm. [SR1]
IR2.	The photometric aperture shall capture 99.5 % of the stellar flux in the NIR and the UV. [SR2, SR3, SR4, SR5]
IR3.	The resolving power shall be at least 3600 for the NIR. [SR6]
IR4.	The resolving power shall be at least 500 for the UV. [SR7]
IR5.	The photometric stability shall be better than 50 ppm (1σ) for the NIR instrument. [SR2, SR3, SR4, SR5]
IR6.	The photometric stability shall be better than 1 % (1σ) for the UV. [SR2, SR3, SR4, SR5]
IR7.	The signal-to-noise ratio of the transition contrast shall be at least 8 for NIR. [SR2, SR3, SR4, SR5]
IR8.	The signal-to-noise ratio of the transition contrast shall be at least 4 for UV. [SR2, SR3, SR4, SR5]
IR9.	The spacecraft shall additionally perform simultaneous observation in VIS $(652 - 660) \pm 0.05$ nm. [SR1]

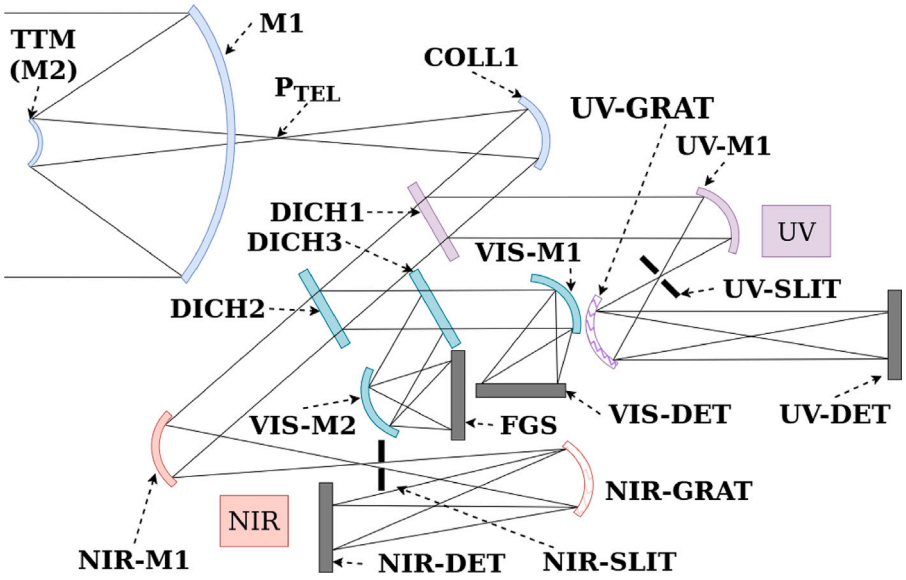

Fig. 6. The optical layout of the UV, NIR, and VIS instrument for the Aetheras mission. Starting from the upper left, starlight is guided through the main mirror (M1) via a tip-tilt mirror (M2) to a collimator (COLL1). The light is split into UV and VIS spectral bands at the respective dichroic mirrors (DICH1 and DICH2). The UV and NIR bands are passed through a slit onto a grating to split them up into a spectral image that is projected onto a detector respectively. Another dichroic mirror (DICH3) splits the image into the fine guidance system and the VIS channel.

Table 2
Aetheras Mission Telescope and Instrument Parameters.

M1	1.5 m
Angular FOV	3.14°
NIR Channel	1070 nm to 1090 nm
	Throughput: 34.01 %
	Spectral Resolution: > 3724
UV Channel	115 nm to 285 nm
	Throughput: 12.96 %
	Spectral Resolution: 571
Compressed Data Rate	28.0 Gbit d^{-1} (20 h operations)

Table 3
Efficiency values for UV, IR, VIS, and FGS channels of the proposed optical path along with overall throughput percentages.

Efficiency	UV	IR	VIS	FGS
Primary Mirror	70 %	90 %	90 %	90 %
Primary Collimator	70 %	90 %	90 %	90 %
UV Dichroic	90 %	90 %	90 %	90 %
UV Slit Focus	98 %			
UV Slit	98 %			
UV Grating Collimator	68 %			
UV Detector Quantum	45 %			
VIS-IR Dichroic		92 %	92 %	92 %
IR Slit Focus		98 %		
IR Slit		98 %		
IR Grating Collimator		88 %		
IR Detector Quantum		60 %		
VIS-FGS Dichroic			92 %	92 %
VIS Focus			98 %	
VIS Detector Quantum			60 %	
FGS Colour Filter				89 %
FGS Focus				98 %
FGS Detector Quantum				60 %
Throughput	12.96 %	34.01 %	36.28 %	32.29 %

resolution of 571 and a two-pixel wide point spread function at full-width half maximum. Additionally, with a 0.22 mm slit in front of the detector, a minimum vertical size of 17 pixels is needed to image the entire slit width.

To achieve a flux resolution of 1 % a minimum pixel depth of 8 bits is required for the given pixel size, as the minimum bin amount is 200. This ensures that even the lowest proposed star flux level, which provides 75.7 photons per second after the presented optical path to the detector, can be observed. Furthermore, to ensure accuracy, the detector should be thermally stabilised. A data rate of approximately 0.155 Mbit per measurement is being expected.

7.4. NIR detector considerations

Infrared detectors have been developed further in recent years to detect stars further into the universe's history. To achieve low enough dark currents with reasonable noise levels, HgCdTe avalanche photodiodes are proposed as NIR detector technology. Observations for astrophysical applications can already be achieved by detectors thermally controlled to 120 K [114].

With a pixel size of 10 µm a NIR detector consisting of a matrix of 7448 × 49 pixels can be derived to cover the spectral range of 1070 nm to 1090 nm and the entire slit width. For the faintest target star IR flux of 6.78×10^{11} photons per second with a resolution of 0.005 % a minimum amount of 40000 flux bins is needed for the given pixel size, resulting in a minimum bit depth of 16 bits. Depending on the final chosen hardware, the light path should be optimised to use the full length of the detector. With currently available technology, resolutions around 5000 are feasible. Thus, the given detector size should be treated as a lower bound.

Given the higher flux in the NIR wavelength domain compared to the UV, the NIR detector allows for enhanced resolution. Efficient cooling is imperative to minimise noise interference in the detector. The average data output from this detector is approximately 5.84 Mbit per measurement.

7.5. VIS and FGS

The VIS channel is filtered to a narrow light spectrum to a 8 nm band around 656 nm [115]. The detector itself can be matched with the fine guidance detector.

For accurate and stable positioning of the target onto the respective detector slit, a feedback loop between the FGS channel detector and the tip-tilt mirror has to be used. This is crucial for maintaining precise alignment between the detectors. The image of the target stars is continuously compared to the projected dot positions on both instruments to minimise the point spread function jitter on the respective spectrometer. Additionally, all detectors and mirror systems should be placed onto one optical bench with known thermal coefficients and distances. For simplicity, the VIS and FGS channels could also be combined into one instrument.

7.6. Additional possible observations

In addition to the required absorption spectral lines, the instrument presented is also capable of observing other important spectral lines such as H_2O, O, O_3, Si-I, and Si-III. These lines provide valuable information about the composition and characteristics of exoplanet atmospheres.

With the addition of H_2O lines to Aetheras' data, insights into atmospheric water vapour can be obtained. Similarly, the observation of O and O_3 lines provides critical information about oxygen content. These two factors are key to assessing habitability and overall atmospheric composition of exoplanets respectively. Si-I and Si-III lines will enable a deeper understanding of silicon-related compounds in exoplanet atmospheres. Overall, the additional observations that Aetheras is capable of can significantly broaden the mission's scientific scope, allowing for a more thorough comprehensive study of exoplanet atmospheres and enhancing our understanding of planetary formation and evolution.

8. Mission analysis

As near UV asymmetries in the transit spectra cannot be seen by ground based telescopes the mission is set to be conducted in space [116]. A mission analysis has been conducted to identify the needed orbit of the mission as well as the different phases to achieve the desired mission goals.

8.1. Mission requirements

Earth geocoronal emission contamination has been a significant concern in previous observations [37]. The geocorona extends more than 38 R_E, as demonstrated by a Ly-α image of the Earth taken from 0.1 AU with the Proximate Object Close Flyby with Optical Navigation (PROCYON) spacecraft [117]. Therefore, an orbit beyond Earth's influence is necessary to create conditions suitable for observing low-emission targets.

Table 4
Aetheras Mission Requirements [MR].

MR1.	The mission shall be conducted at least 38 Earth radii away from Earth to be outside Earth's exosphere. [IR1, IR2, IR8, IR9, IR10]
MR2.	The mission shall provide a total scientific observation time of at least 12 000 h. [SR2, SR4]
MR3.	The mission shall first observe the primary targets and afterwards observe the secondary targets. [SR2]
MR4.	The instrument bore sight shall not be pointed within a 15° cone towards the Sun during operations. [SR2, SR3, SR4, SR5]
MR5.	The instrument shall be pointed with a pointing accuracy of 7 milli arcsec with a stability of 5 % over at least 10 h towards the targets. [SR2, SR3, SR4, SR5]

Considering an average observation time of 10 h and four transits per target, along with a minimum of 300 observed targets, a baseline scientific observation time of 12 000 h is derived. The target count preemptively incorporates a margin to accommodate potential future detections by other missions. The required observation time may vary significantly for specific targets.

The Mission Requirements are detailed in Table 4.

To minimise space debris risks for future missions, an additional mission constraint has been imposed: the spacecraft shall enter a graveyard orbit at the end of its decommissioning phase.

8.2. Orbit and mission phases

A Lissajous orbit around the Lagrange point L2 of the Earth–Sun system has been selected. This orbit not only places the spacecraft outside the geocorona but also provides a low thermal noise environment for the NIR detector and offers good sky coverage for observations. The orbit has been designed to ensure that the spacecraft remains free from any eclipses.

Following a burn towards L2, the satellite will detach from its launcher and deploy. This burn is strategically designed to consistently undershoot the trajectory, ensuring that the spacecraft always points away from the sun during correction burns.

After separation, the spacecraft will actively align itself to enable the solar panels to pass the sun while avoiding direct sunlight on the detectors. Once basic commissioning of the platform is completed, the cruise phase towards L2 is initiated. The transfer to L2 will span 60 days, incorporating a manoeuvre for launcher injection corrections, along with an L2 direct injection of around 50 $m\,s^{-1}$ along the way. Upon reaching L2, the science payload section as well as the platform undergoes detailed commissioning.

The nominal observation phase is scheduled to last 3 years. At least one year will be used to observe the targets presented in Section 4. The additional observation time is to revisit those targets and open call targets which may arise also from discoveries made with space telescopes like PLATO. Throughout its operational lifetime, station-keeping activities will involve both orbit and attitude maintenance. Post-observation, the spacecraft is to be decommissioned into an unstable outbound orbit, positioned far from Earth.

9. Spacecraft design

Both the mission objectives and the payload specifications necessitate certain requirements, shaping the design parameters for the spacecraft. The subsequent sections elaborate on the envisioned satellite design for the Aetheras mission.

Table 5
Aetheras Mission System Requirements [SReq].

SReq1.	The spacecraft shall be 3-axis stabilised with a pointing accuracy of 7 milli arcsec with a stability of 5 % over at least 10 h. [IR5, IR6, IR7, IR8]
SReq2.	The spacecraft shall have a propulsion system to perform orbit insertion, station keeping for at least 3 years, and disposal. [MR1, MC3]
SReq3.	The spacecraft shall withstand the radiation environment at the target orbit for at least 3 years. [MR1]
SReq4.	The spacecraft shall be able to observe targets between [−70°, 80°] in declination with respect to the ecliptic. [SR2, SR3, SR4]
SReq5.	The spacecraft shall shield the instruments from stray light. [IR7, IR8, MR4]
SReq6.	The spacecraft shall be able to store at least 26.4 Gbit of data for at least 2 days. [SR5, SR7, IR1]
SReq7.	The spacecraft shall provide the necessary electrical power for all operational modes. [MR2, MR3]
SReq8.	The spacecraft shall provide a thermal system for the NIR that keeps the detector area at a temperature lower than 130 K and a stable temperature environment for the optics as well as the UV detector with a maximum deviation of 1°Celsius. [MR4, MR5]

9.1. System requirements

Eight top-level system requirements are identified, which dictate the specifications of the subsystems the most, as detailed in Table 5. The subsequent sections delve into a detailed discussion of the subsystems that address these requirements.

To achieve stable observations, the platform must maintain stability both in attitude and thermal conditions. Limiting the sunlight exposure on the detectors is crucial, and additional measures, such as stray light shielding, are implemented to ensure low-noise observations.

9.2. Operational modes

Different operating modes are used according to the needs during different phases of the mission. The following six modes represent simplified states and serve system scaling purposes:

Launch mode (LAU): Encompasses the period from launcher separation to achieving stable attitude and telemetry.

Manoeuvre mode (MAN): Includes all manoeuvres requiring the use of orbital control thrusters.

Commissioning and testing mode (TES): Combines the platform and instrument commissioning and validation processes. Note that this mode is unsuitable for scaling, as it does not reflect the chronological sequence of system tests.

Cruise mode (CRU): Active between orbit injection and arrival at L2, during which the spacecraft operates in a low-power hibernation mode.

Science and communication mode (SCM): Encompasses nominal operations during scientific observations in orbit around L2.

Safe mode (SAF): Reserved for recovery from abnormal scenarios, activating only essential and mission-saving systems.

9.3. Attitude and orbit determination and control

With the mission performing precise measurements of distant targets, the Attitude and Orbit Determination and Control System (AODCS) is crucial not only in maintaining the desired orbit but also for precise pointing towards the target. The next sections will give an overview of the calculations and design considerations needed for the propulsion system as well as for attitude control.

9.3.1. Propulsion

From the preliminary trajectory discussed in Section 8, a total Δv budget of $125.8\,\mathrm{m\,s^{-1}}$ is derived as seen in Table 6. The biggest contributors are the needed launch error correction manoeuvres as well as the burn needed to bring the spacecraft into a graveyard orbit, which ensures that the orbits around L2 will be free of debris for at least 100 years after the spacecraft decommissioning.

For orbit manoeuvres, three 20 N Hydrazine thrusters [119] are chosen, along with up to 176 L fuel tank [120], capable of holding the required 68 kg of Hydrazine as calculated from the Δv budget and additional fuel for attitude maintenance as those thrusters use the same propellant.

The tank is intentionally oversized, allowing for the possibility of loading more fuel if the launcher budget permits, thereby potentially extending the mission lifetime, as this is the only consumable on board.

In future design iterations, it is advisable to consider similar systems that use less harmful propellants, such as those under development by ECAPS [121,122].

The three orbit maintenance thrusters are strategically positioned in a line along the bottom of the spacecraft, providing redundancy and assistance during attitude changes. A single thruster is sufficient to deliver the necessary impulse for all manoeuvres. In the event of a failure in the middle thruster, the outer ones can perform the burns. Suppose two thrusters (for instance, the middle and one outer) cannot be operated. In that case, orbital manoeuvres must be executed using the remaining thrusters in conjunction with the attitude thrusters to counter the offset towards the centre of mass.

9.3.2. Attitude determination and control

For this mission, an attitude determination system comprising of two star tracker compute units with two tracking heads each, an inertial measurement unit, and six sun sensors is proposed to gain attitude knowledge with up to 0.6 arcsec precision [123–125]. This system provides redundancy through multiple units or utilises the built-in redundancy features of the selected devices. The selected attitude computer (ICDE NG by Airbus Defence and Space [126]) processes additional fine guidance information from the VIS instrument of the payload, combined with data from these sensors, to deliver the necessary attitude information to all other systems.

For main attitude and stability control, four reaction wheels are employed in a tetrahedral configuration. To enable stable observations lasting up to 10 h without interruption, a momentum storage of at least 8 N m s is required. Hence, reaction wheels with up to 18 N m s momentum storage are selected for this baseline design [127]. Twelve 1 N attitude control thrusters are used to dissipate the momentum accumulated during observations [128]. Only eight thrusters are needed to perform all manoeuvres, with the additional four providing redundancy. The needed Hydrazine fuel of 12 kg for momentum dumping over the mission life of three years can be stored in the same as the fuel for the orbital manoeuvres.

9.4. On-board data handling

The on-board data handling organises the transfer and storing of payload, telemetry, and subsystem housekeeping data between the different instruments. The data handling of the payloads is done by their dedicated data processing units (DPU) which also have a connection to the central computing unit (CCU) as depicted in Fig. 7. Avionics systems namely attitude and orbit determination and control system (AODCS), electrical power system (EPS) and telecommunication (COM) are connected via a bus system to ensure commanding even if the compute unit is malfunctioning. The COM can address messages to other systems than the CCU if needed. All data connections are double-redundant to mitigate connection issues.

Due to a limited communication window, the data is temporarily stored on-board before transmission to the ground. With redundancies, onboard storage must handle at least 44 Gbit/day of raw science and telemetry data for at least two days. The buffer has to be at least 40 Mbit based on the expected data rate for one minute and will be scrubbed regularly to limit the impact of Single Event Effects (SEEs). A computing unit capable of telemetry data transmission up to 10 Mbit, coupled with external storage of up to 4 TB useable capacity, can handle more than sufficient data backup needs for this mission [129,130]

Table 6
Δv Budget for the Aetheras mission, including manoeuvres after spacecraft separation from the launcher until disposal to a graveyard orbit. Perigee velocity variation compensation and removal of launcher dispersion are worst case estimates. Delta-V margins have been applied according to mission design recommendations by ESA [118]: 5 % for accurately calculated manoeuvres (including trajectory and detailed orbit maintenance manoeuvres), 100 % for general orbit maintenance manoeuvres not analytically derived, and 100 % for attitude control and angular momentum management manoeuvres.

Manoeuvre	Δv [m s^{-1}]	Margin [%]	Margin [m s^{-1}]	Total [m s^{-1}]
Compensation for Perigee Velocity variation	26	5	1.3	27.3
Removal of Launcher Dispersion	50	5	2.5	52.5
Orbit Maintenance (3 year)	3.0	100	3	6
Injection into unstable outbound orbit	20	100	20	40
Total with margin				125.8

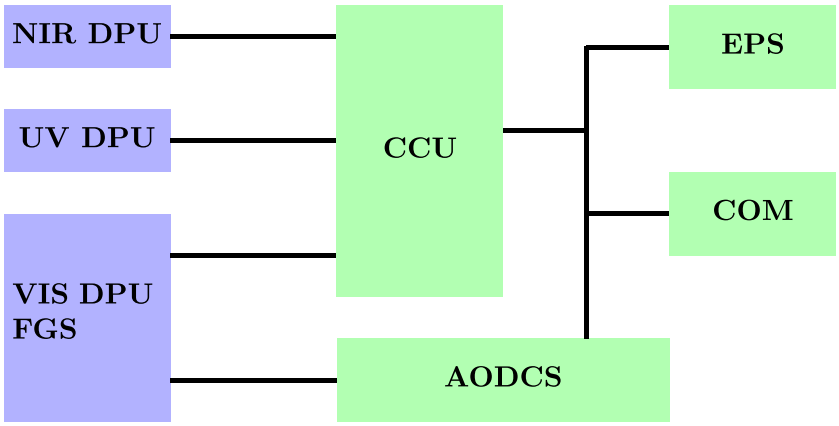

Fig. 7. On-board bus architecture of the Aetheras mission. Data processing units (DPU) of the different payloads are connected to a central computing unit (CCU). The visual fine guidance system (FGS) has also a direct link to the AODCS to get current attitude data. AODCS, OBDH, EPS and COM share a common bus communication.

9.5. Telecommunication

The spacecraft utilises X-Band with a bandwidth of 10 MHz as the primary downlink to Earth for transmitting science data. A 0.5 m antenna dish can achieve a gain of up to 32 dB which is mounted on a fully integrated antenna pointing mechanism currently under development from Airbus [131]. The power amplifier, with a typical output of 17 W, and a corresponding radio are modelled using products provided by General Dynamics [132,133]. Both components are redundantly incorporated into the system.

In addition to the X-Band, a redundant S-Band system ensures omnidirectional coverage for telecommand uplinking. Four omnidirectional S-Band antennas, along with two amplifiers and an internal redundant radio (also by General Dynamics) [134,135], are employed. The multifunctional radio supports telemetry rates up to 8 Mbit s^{-1} with QPSK encoding. This system can also serve as a backup for science downlink with a significantly reduced data rate.

For data downlink, the 15 m antennas of ESA's ESTRACK network (KIRUNA-1 and KURUU-1) can be utilised to achieve high data rates up to 6 Mbit s^{-1}. Smaller antennas may also be employed for telecommands via S-Band. The S and X-Band link budgets, assuming the above-mentioned ground stations for X-Band and a generic 5 m antenna for S-Band, are presented in Table 7.

Overall, a link margin of more than 6 dB is ensured throughout the mission, which is well above the required margin of 3 dB as required by ESA [118]. With a data rate of 6 Mbit s^{-1} for the X-Band, and considering the anticipated scientific data production of 28.0 Gbit d^{-1}, the minimum required communication window is less than 80 min d^{-1}. In the case that the science data has to be downloaded via the S-Band a different observation strategy is recommended as the data rate is too low to download a whole day of science data.

Table 7
Link budget of Aetheras spacecraft equipped with a high gain X-Band antenna and low gain S-Band antennas. 15 m antennas of ESA's ESTRACK network (KIRUNA-1 and KURUU-1) and 5 m generic ground station are used as ground stations for X-Band and S-Band respectively.

	Uplink		Downlink	
Frequency	8.5 GHz	2.1 GHz	7.2 GHz	1.7 GHz
Transmission Loss	−236.4 dB	−224.3 dB	−235.0 dB	−222.4 dB
TX Transmit Power	100 W	250 W	17 W	8.3 W
TX Antenna Gain	50.9 dB	38.7 dB	29.5 dB	2.9 dB
EIRP	69.9 dB	61.8 dB	41.0 dB	11.4 dB
RX Antenna Gain	30.9 dB	4.8 dB	59.0 dB	46.5 dB
Receiver G/T	9.1 dB	−17 dB	39.5 dB	26.9 dB
Data rate	12 Mbit s^{-1}	10 kbit s^{-1}	6 Mbit s^{-1}	7 kbit s^{-1}
Final E_b/E_n	9.3 dB	9.0 dB	6.3 dB	6.0 dB

9.6. Data packages and commanding

Two distinct data centres are founded for this mission: A commanding data centre and a science data centre. After the telemetry and science data packages are successfully received on Earth via frequency-specific ground station networks from ESA, the commanding data centre will handle all spacecraft health and subsystem-related tasks. Configuring the spacecraft for the different mission phases as well as executing all the commands needed to perform a scientific observation requested by the science data centre.

After the measurement data are retrieved they will be sent to the science data centre as seen in Fig. 8 to be cleaned up and checked for its integrity to prepare data products that can be made available. For each observation the user will get the following timestamped data packages: Host star spectrum and visual image, exoplanet spectra for ingress,

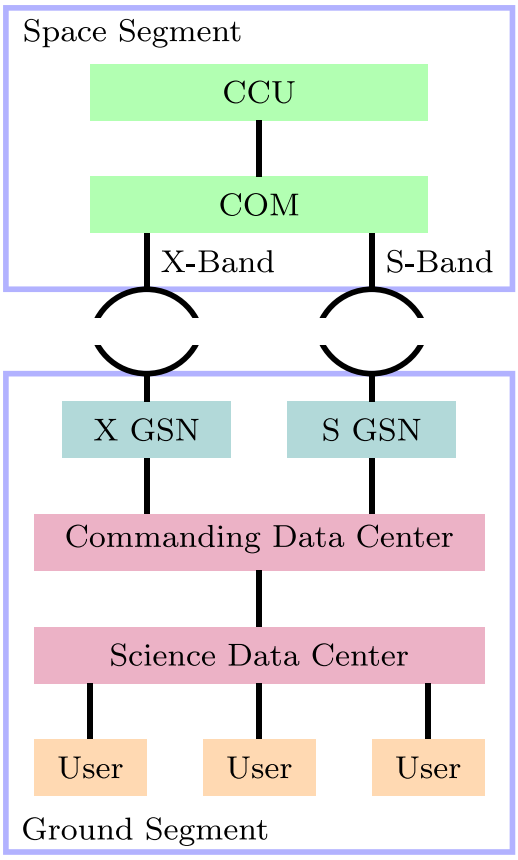

Fig. 8. Data flow of the Aetheras mission. Science and telemetry data stored at the CCU gets transferred to the COM system. Telemetry data will get sent via S-Band to the ground station network (GSN). X-Band is used to transmit science data to a dedicated GSN. Data from both GSNs gets processed at the commanding data centre. Science data will be processed and stored at the science data centre to be made available to the users.

egress and during transit. Spectral data packages will be subdivided into NIR and UV sub-packages.

The data can be retrieved by the science community from servers hosted by the science data centre. At first, all primary collaborators including instrument providers will get access. After one year of exclusive access, the data will be publicly available to enable a wider science community to participate.

9.7. Thermal management

To ensure the reliable and consistent performance of Aetheras in all required cases, a top-level thermal analysis is performed. Key parameters to consider in the thermal analysis are defined by the critical spacecraft components onboard Aetheras. In particular, the NIR detector has an optimal range of only 118 K to 122 K (SReq8) during operation. The batteries and fuel mostly drive the spacecraft system's thermal requirements to avoid charging problems and ignition delays [136,137]. A summary of the most important temperature ranges is given in Table 8. A sunshield, a radiator, a baffle, thermal coatings, and heaters are implemented in different areas to ensure these requirements are met. The spacecraft is divided into hot and cold sections, with components with a larger thermal range placed in between the two sections. This allows the components to be within optimum thermal range while also acting as a heat sink to isolate the hot and cold sections.

Table 8
Thermal operating ranges for most critical spacecraft components onboard Aetheras.

Component	Thermal Range
Battery	283 K to 333 K
Fuel	288 K to 313 K
NIR detector	118 K to 122 K
UV detector	293 K to 303 K
UV optical mirror	283 K ± 1 % rms

The hot section is referred to as the service module. The cold section, which contains the telescope, is referred to as the payload section (see Section 9.9).

For thermal energy emission it is assumed that all electric power is dissipated as heat by the respective component. The only power not full converted to heat is power used for communication antennae. Different operating modes, as seen in Section 9.8, are taken into account. The case in which the spacecraft rotates to expose the thermally unprotected side is not considered, as this is regarded as a mission failure due to the telescope then being exposed to the sun, compromising the required function. It must be noted that it might be possible to recover from this state with enough waiting time after the spacecraft has been brought into an attitude in which the sun is not facing the telescope. For all calculations, a solar flux value for a perihelion Earth–Sun L2 distance is taken as external input. Calculations follow Stefan Boltzmann's law.

The sunshield consisting of four layers of AlSiO coated 25.4 µm Kapton film is placed in between the Sun and the payload section. Gaps of void in between create a radiative thermal resistance [138]. Due to the NIR detector's optimal thermal range, the requirement of the sunshield is set to reduce the temperature of the cold section of the spacecraft to 120 K. This design results in a final thermal temperature of 118.45 K on the outer spacecraft surface. Apart from the ability to comply with the thermal requirements, the AlSiO coating is chosen to increase the longevity of the sunshield against heating cycles and performance degradation [139].

A Radiator is used on a part of the cold section of the spacecraft. This radiator will be constructed similar to the system used on the Hubble satellite or the more recent satellite Euclid [140–142]. The radiator placement allows for the removal of heat from components in between the hot and cold sections. This contributes towards the thermal isolation of the hot and cold sections [140,143]. Heat created by the components within the cold section is emitted via this radiator system, ensuring no risk of exceeding optimal thermal ranges.

The Baffle further reduces thermal stress during normal operation by shielding the telescope from stray light. As a result, this prevents any unwanted thermal input via the telescope. A thermal coating of Chemglaze Black Paint Z306 is chosen for application on the service module. This creates a stable thermal environment within the service module. The material is chosen by using various emissivity and absorptivity values in the Stefan Boltzmann law calculations of final temperate. An experimental approach is taken to arrive at the material choice Chemglaze Black Paint Z306, using supplier material catalogues [144,145]. Chemglaze Black Paint Z306 has an emissivity of 0.90 and absorptivity of 0.95 [145]. This results in an upper temperature limit of 300.2 K and lower temperature limit of 295.9 K in the service module.

9.8. Electrical power

Considering the payload and essential onboard systems, the spacecraft design mandates a minimum continuous power output of 687 W in SCM mode as seen in Table 9. This mode serves as the reference for power conditioning scaling. The power budget is calculated with duty cycles, redundancies and margins in mind.

Table 9
Power budget for different spacecraft modes of the Aetheras mission. Subsystem values are shown with duty cycle and redundancy considerations in mind. Maturity margins have been applied according to current ESA recommendations [118]: 5 % for "Off-The-Shelf" items, 10 % for "Off-The-Shelf" items requiring minor modifications and 20 % for new designed/developed items, or items requiring major modifications or re-design. An additional margin of 30 % is applied to the total power of each mode.

Subsystem	MAN [W]	TES [W]	SAF [W]	CRU [W]	LAU [W]	SCM [W]
Payloads	3.1	29.6				29.6
Attitude Det. and Control	290.3	290.1	149.4	271.2	149.4	290.4
Propulsion	49.5					
On-Board Data Handling	49.4	49.4	49.4	49.4	26.3	49.4
Communication	14.2	30.3	16.3	12.9	16.3	55.4
Mechanisms		0.3				0.3
Power	84.0	84.0	84.0	84.0	84.0	84.0
Thermal	19.2	19.2	24.0	24.0	12.0	19.2
Total power	662.5	653.8	420.0	573.9	374.4	**686.8**

The LAU mode is used for battery sizing, taking into account the absence of eclipses in the planned trajectory. In this mode, the spacecraft must initially orient itself towards the sun and initiate all required systems without relying on primary power production from the solar panels.

The modular power conditioning unit LEO PCDU EVO by Airbus delivers a 28 V system bus for the entire spacecraft and can handle single component loads up to around 300 W [146].

For a safe mode operation lasting at least 2 h, two 512 W h VES16 8s4p batteries by Saft in a redundant setup are sufficient [147]. The calculations take into account a depth of discharge of 74.9 %, which is high as the batteries are not in heavy use after the spacecraft is stabilised.

To meet the power demands, the calculated solar panel area required is 2.84 m^2 assuming Azur Space 3G30 A solar cells [148]. The total power output of 895 cells reaches a maximum of 687 W. This value is adjusted to account for various factors such as degradation of solar panels from radiation, maximum power point tracking (MPPT) efficiency of 98 %, battery charge regulator (BCR) efficiency of 90 %, and cell loss at maximum temperature as well as a 30° angle towards the sun.

9.9. Configuration

As all subsystems are defined, a preliminary system configuration and payload integration are conducted. The spacecraft can be divided into two sections: A payload section houses the telescope and the optical instruments. Underneath, a service module section contains the supporting subsystems that have been laid out above. This design is a first layout work of the different components in side the preliminary structure of 1.84 m × 1.8 m × 3.42 m.

The service module is depicted from below in Fig. 9. Systems are modelled after their envelope given in the respective datasheet. A tetrahedral support structure is introduced in the centre to provide mounting surfaces for the reaction wheel arrangement. All systems locations are selected with the centre of mass as well as their thermal and system internal requirements in mind.

Figs. 10(a) and 10(b) show the internal layout from the side and the deployed structure respectively. The solar panel is fixed on the sides centre facing the Sun and serves as the first light and heat shield. Additionally, the baffle and a radiator surface help to meet thermal and stray light requirements. The fuel tank extents in the centre into the volume covered by the radiator surface. The X-Band antenna is placed on an actuation arm to enable downlink also during off axis measurement times.

The instruments light path is shown in a preliminary layout. For a more detailed layout, an optical simulation of the entire instrument needs to be done. A design for an optical bench to ensure precise alignment of all optical parts is still needed. Ideally the radiator surface is placed as close to the components needing cooling. It becomes clear that the payload section can be further optimised potentially leading to a smaller spacecraft. This design also misses some structural support components needed to fasten components into place (see Fig. 10).

Table 10
Mass Budget of the Aetheras mission with contingency and total combined masses for each subsystem. Maturity margins have been applied according to current ESA recommendations [118]: 5 % for "Off-The-Shelf" items, 10 % for "Off-The-Shelf" items requiring minor modifications and 20 % for new designed/developed items, or items requiring major modifications or re-design.

Subsystem	Mass [kg]	Cont. [kg]	Comb. [kg]
Payloads	297	59	357
ADCS	75	5	79
Propulsion	36	6	42
OBDH	13	1	14
COM	23	5	27
Power	41	4	45
Thermal	50	10	60
Structure	250	50	300
Dry Mass			926

With the configuration shown the dry mass as presented in Table 10 is 926 kg. With a 20 % system margin and assuming that the harness is around 10 % of the dry mass the total dry mass is 1220 kg.

A combined ADCS and orbit maintenance fuel of 82 kg has to be added. This gives a total wet mass of the spacecraft of 1302 kg.

The spacecraft fits within the payload capacities of various currently available launchers, considering both its mass and volume specifications. For this proposal, the Ariane 62 launcher is chosen due to the availability of extensive documentation. The Ariane 62 is capable of delivering payloads of up to 2600 kg to a trajectory towards L2.

Assuming a launcher-side launch adapter (e.g. PLA6 1194) weight of 71 kg [149], the total mass launched is 1373 kg. The spacecraft fits into the lower compartment of the launch bay of the Ariane launcher family, leaving the upper compartment available for potential utilisation.

10. Feasibility

For the mission to be viable, it has to be feasible from a technological and risk management perspective. There are several identified risks with the Aetheras mission.

Firstly, mechanical damage, production deficits, and instrument contamination of the telescope may slow down the project significantly as extensive vibrational testing and component monitoring have to be conducted in high ISO class clean rooms. Secondly, Aetheras may be unable to detect intended proxies due to unanticipated effects of the host star or the interstellar medium. However, this is mitigated by additional proxies observed in different spectral ranges, which are already built into the current instrument design.

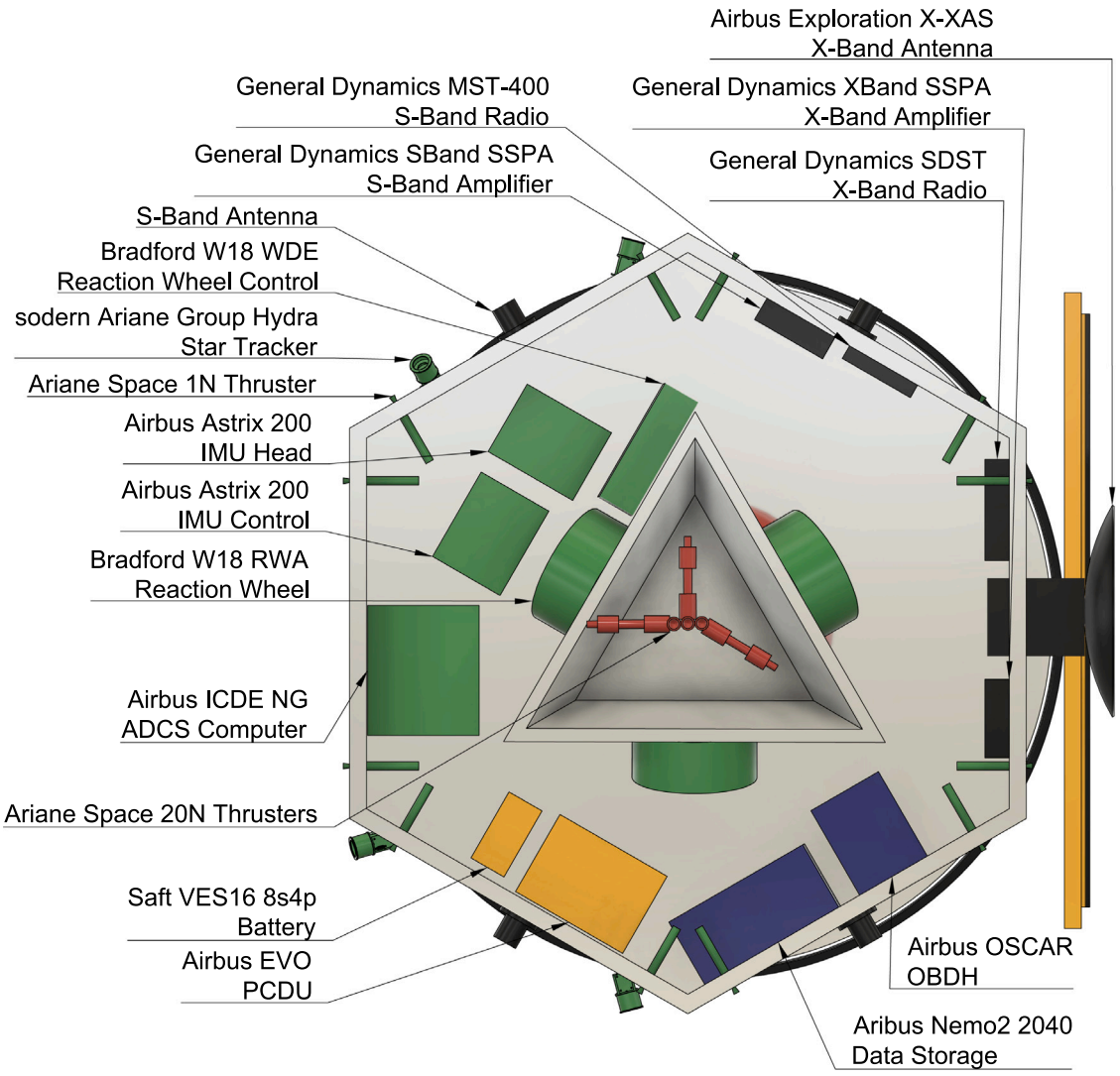

Fig. 9. Aetheras Service Module: The bottom of the service module has been removed in this view to allow visibility to the internal parts. Parts are colour coded with respect to the system they belong to: Green: ADCS, Blue: OBDH, Yellow: Power, Black: COM, Red: Propulsion.

Table 11
TRLs of the payload components.

TRL	PAYLOAD
4	Telescope & Optics
3	UV instrument
5	NIR instrument
5	VIS instrument

Finally, a mission delay due to too low component TRLs at later stages of the project is considered. The current TRLs for the critical components are shown in Table 11. Most notable are the low TRL levels of the optical bench and the UV instrument. Due to new technologies used, significant effort has to be made to raise the TRL levels of the detector technologies. The optical path is a unique build for this instrument and thus requires testing of all interconnected parts [105,106,108]. However, similar instruments have been made in the past, building confidence that the proposed design is feasible [110,111,114,150,151].

Teledyne offers the H4RG-10 detector for NIR selected for use in the Roman Space Telescope [151]. If two of these are used in parallel, one can cover the required pixel space of Aetheras. This particular variant has not been used in space. Instead, the variant with larger pixel pitch is used on the ISS [152]. Therefore, a low TRL level is assigned to the proposed Aetheras NIR solution. A potential candidate for the UV detector is a custom-fabricated Teledyne CCD201-20, as it has been shown to provide the needed quantum efficiencies [150]. As this is not a product with heritage, one has to consider significantly lower TRL as well as development risks. A potential candidate for the visible spectrum with already proven flight heritage is the Teledyne CCD47-20 sensor [153].

Early testing of the telescope and the related optical and instrumental systems is necessary to keep track of the current development status of the project. The risks associated with service module systems are quite low as they are modelled after already flown hardware. Therefore, such risk is not considered in this first order risk assessment.

11. Cost

A preliminary budget is calculated for this mission, which can be seen in Table 12. Significant development costs are considered for the optics and payload system. As the service module is modelled after already existing or late-stage development hardware, lower costs are been identified.

This budget includes the support for several scientists for 4 years to conduct the data analysis. Launcher costs assume an Ariane 62

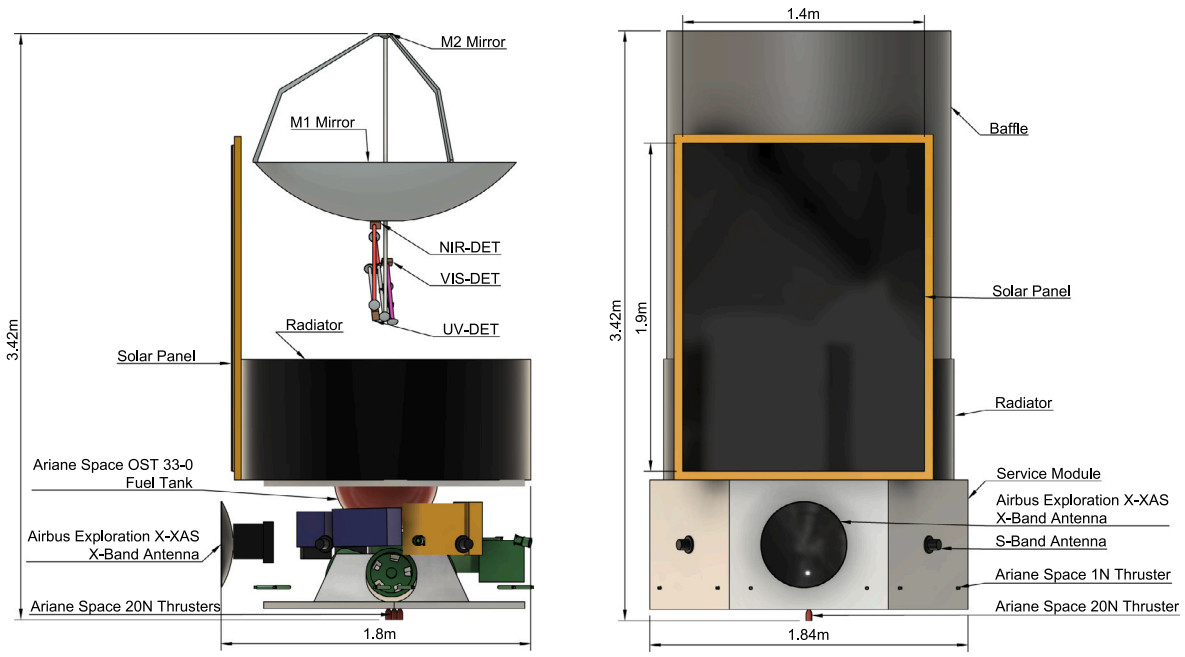

(a) View with baffle and service module walls removed for better visibility.

(b) View in fully deployed state as seen from the direction of the sun in orbit.

Fig. 10. Aetheras Satellite Side Views: The service module on the bottom provides all the necessary power and data connections to the telescope payload section on the top. Parts are colour coded with respect to the system they belong to: Green: ADCS, Blue: OBDH, Yellow: Power, Black: COM, Red: Propulsion.

Table 12
Spacecraft costs.

Item	Cost [M€]
Telescope	150
UV Instrument	80
NIR Instrument	50
VIS Instrument	30
Service Module	150
Development/AIT	120
Data analysis	30
Launcher	75
Total cost with 20 % margin	822

rocket with no additional payloads. According to ESA classification, the mission fits the criteria of an L-class mission, reaching 822 million euros including a 20 % margin.

12. Future work

This study highlighted several key areas that require more attention in the future. Firstly, the current instrumentation needs further refinement with respect to the exact optics calculations to improve the design of the optical bench. Crucial for an instrument revision is also a more detailed thermal analysis, especially of the instrument bay of the spacecraft, as it significantly influences the performance of the telescope and its detectors. This is especially important due to the proximity of the UV and NIR instruments and their different operating temperatures. Additionally, a more detailed observation strategy has to be derived to calculate a more detailed fuel budget and an understanding of the overall schedule. With respect to the VIS channel, the possibility for more than one band pass filter, for example via a filter wheel or a sectioned sensor, could be explored in the future.

13. Conclusion

In summary, the Aetheras mission aims to understand the complex interplay between exoplanetary atmospheres, host stars, and atmospheric escape processes, seeking to answer questions concerning atmospheric escape and its correlation with exoplanet characteristics and their host star properties. Special interest is set to the Radius Valley and the hot Neptune desert, as well as the influence of exoplanetary magnetic fields. The system and instrument requirements have been derived from the given science theme and their desired scientific objectives and observation requirements resulting in a $1.84\,\mathrm{m} \times 1.8\,\mathrm{m} \times 3.42\,\mathrm{m}$ sized spacecraft.

To detect proxies for atmospheric escape and exoplanetary magnetic fields the mission will perform transit spectroscopy in NIR (1070 nm to 1090 nm) and UV (115 nm to 285 nm) with a 1.5 m telescope, which enables the identification of absorption lines in the spectra of transiting exoplanets in front of their host stars.

For this, a satellite is placed in an L2 orbit, communicating with ESA's ground station network. A first analysis of the needed systems and their sizing has been performed based on already existing hardware. The space system has an expected mission lifetime of 3 years and weighs 1302 kg with an expected power consumption of 686.8 W in science mode. The current design's only consumable need is the fuel for orbit maintenance and momentum dumping. Therefore, depending on newly discovered targets as well as the used fuel for orbit insertion, a mission extension is feasible.

A feasibility study shows that challenges related to component technology readiness levels and instrument contamination exist, and must to be further investigated. This is reflected in the presented preliminary budget where a significant share of costs is dedicated to advancing the TRL of the involved instrument technologies.

Overall, the Aetheras mission aims to greatly increase the understanding of the relation between host stars, exoplanets, and atmospheric escape and is capable of much more.

CRediT authorship contribution statement

Marius Anger: Project administration, Writing – original draft, Writing – review & editing, Conceptualization, Data curation, Visualization. **Aksel Søren Beltoft:** Conceptualization. **Federico Biassoni:** Visualization, Validation, Writing – review & editing. **Johanna Noria Brecher:** Data curation, Writing – review & editing, Visualization, Conceptualization. **Antoine Corne:** Writing – original draft, Conceptualization, Data curation. **Jo Ann Egger:** Data curation, Conceptualization. **Simone Filomeno:** Writing – original draft, Conceptualization, Data curation. **Margarida Graça:** Data curation, Conceptualization, Writing – original draft. **Viktoria Keusch:** Data curation, Writing – original draft, Conceptualization. **Guillem Khairy:** Conceptualization, Writing – original draft. **Jakub Kowalczyk:** Writing – original draft, Writing – review & editing, Conceptualization, Visualization. **Riccardo Lasagni Manghi:** Supervision, Conceptualization. **Dominik F. Loidolt:** Writing – review & editing, Conceptualization, Writing – original draft. **Maja Marminge:** Conceptualization, Writing – original draft, Writing – review & editing, Data curation. **Alex McDougall-Page:** Conceptualization, Visualization, Writing – review & editing, Writing – original draft. **Lukas Tamulevicius:** Writing – original draft, Conceptualization. **Elena Tonucci:** Visualization, Conceptualization, Data curation. **Elise Wright Knutsen:** Conceptualization, Visualization, Supervision.

Declaration of competing interest

The authors declare that they have no known competing financial interests or personal relationships that could have appeared to influence the work reported in this paper.

Acknowledgements

Special thanks to Tibor Agocs for his unflinching support. Thank you to Mark Boyd for helping with the thermal analysis. See you starside!

The authors acknowledge funding from the European Space Agency (ESA), France and the Austrian Research Promotion Agency (FFG), which supported Summer School Alpbach 2023, on the theme "Exoplanets - Understanding alien worlds in diverse environments".

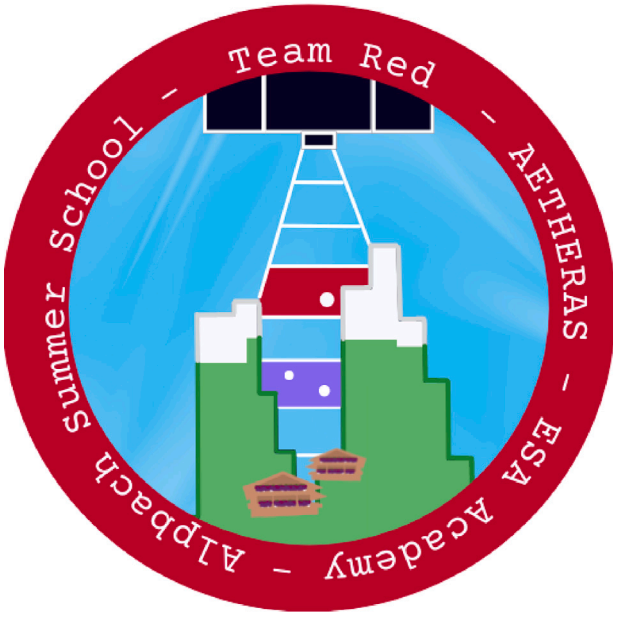

References

[1] NASA Exoplanet Science Institute, Planetary systems table, 2023, URL https://exoplanetarchive.ipac.caltech.edu/.

[2] A.P. Showman, X. Tan, V. Parmentier, Atmospheric dynamics of hot giant planets and brown dwarfs, Space Sci. Rev. (ISSN: 0038-6308) 216 (8) (2020) 1–83, http://dx.doi.org/10.1007/s11214-020-00758-8.

[3] B.J. Fulton, E.A. Petigura, The California-Kepler survey. VII. Precise planet radii leveraging gaia DR2 reveal the stellar mass dependence of the planet radius gap, Astron. J. (ISSN: 1538-3881) 156 (6) (2018) 264, http://dx.doi.org/10.3847/1538-3881/aae828.

[4] P.W. Cauley, E.L. Shkolnik, J. Llama, A.F. Lanza, Magnetic field strengths of hot jupiters from signals of star–planet interactions, Nat. Astron. (ISSN: 2397-3366) 3 (12) (2019) 1128–1134, http://dx.doi.org/10.1038/s41550-019-0840-x.

[5] R.K. Yadav, D.P. Thorngren, Estimating the magnetic field strength in hot jupiters, Astrophys. J. Lett. 849 (1) (2017) L12, http://dx.doi.org/10.3847/2041-8213/aa93fd.

[6] G.B. Trammell, P. Arras, Z.-Y. Li, Hot jupiter magnetospheres, Astrophys. J. 728 (2) (2011) 152, http://dx.doi.org/10.1088/0004-637X/728/2/152.

[7] J.S. Pineda, G. Hallinan, M.M. Kao, A panchromatic view of brown dwarf aurorae, Astrophys. J. 846 (1) (2017) 75, http://dx.doi.org/10.3847/1538-4357/aa8596.

[8] J. Saur, C. Willmes, C. Fischer, A. Wennmacher, L. Roth, A. Youngblood, D.F. Strobel, A. Reiners, Brown dwarfs as ideal candidates for detecting UV aurora outside the solar system: Hubble space telescope observations of 2MASS J1237+6526, Astron. Astrophys. 655 (2021) A75, http://dx.doi.org/10.1051/0004-6361/202040230.

[9] D.A. Ruíz-Rodríguez, L.A. Cieza, S. Casassus, V. Almendros-Abad, P. Jofré, K. Muzic, K.P. Ramirez, G. Batalla-Falcon, M.M. Dunham, C. González-Ruilova, A. Hales, E. Humphreys, P.H. Nogueira, C. Paladini, J. Tobin, J.P. Williams, A. Zurlo, Discovery of a brown dwarf with quasi-spherical mass loss, Astrophys. J. 938 (1) (2022) 54, http://dx.doi.org/10.3847/1538-4357/ac8ff5.

[10] S. Hazra, O. Cohen, I.V. Sokolov, Exoplanet radio transits as a probe for exoplanetary magnetic fields—Time-dependent MHD simulations, Astrophys. J. 936 (2) (2022) 144, http://dx.doi.org/10.3847/1538-4357/ac8978.

[11] X. Zhang, Atmospheric regimes and trends on exoplanets and brown dwarfs, Res. Astron. Astrophys. 20 (7) (2020) 099, http://dx.doi.org/10.1088/1674-4527/20/7/99.

[12] B. Lavie, Atmospheric Studies of Brown-Dwarfs and Exoplanets: Insights into Planet Formation and Evolution (Ph.D. thesis), University of Geneva, Switzerland, 2018, http://dx.doi.org/10.13097/archive-ouverte/unige:136544.

[13] G.W. Marcy, R.P. Butler, Planets orbiting other suns1,2, Publ. Astron. Soc. Pac. 112 (768) (2000) 137, http://dx.doi.org/10.1086/316516.

[14] C. McCarthy, B. Zuckerman, The brown dwarf desert at 75-1200 AU, Astron. J. 127 (5) (2004) 2871, http://dx.doi.org/10.1086/383559.

[15] N. Unger, D. Ségransan, D. Barbato, J.-B. Delisle, J. Sahlmann, B. Holl, S. Udry, Exploring the brown dwarf desert with precision radial velocities and gaia DR3 astrometric orbits, Astron. Astrophys. 680 (2023) A16, http://dx.doi.org/10.1051/0004-6361/202347578.

[16] A.T. Stevenson, C.A. Haswell, J.R. Barnes, J.K. Barstow, Combing the brown dwarf desert with Gaia DR3, Mon. Not. R. Astron. Soc. (ISSN: 0035-8711) 526 (4) (2023) 5155–5171, http://dx.doi.org/10.1093/mnras/stad3041.

[17] P.J. Armitage, I.A. Bonnell, The brown dwarf desert as a consequence of orbital migration, Mon. Not. R. Astron. Soc. (ISSN: 0035-8711) 330 (1) (2002) L11–L14, http://dx.doi.org/10.1046/j.1365-8711.2002.05213.x.

[18] P.H. Jumper, R.T. Fisher, Shaping the brown dwarf desert: predicting the primordial brown dwarf binary distributions from turbulent fragmentation, Astrophys. J. 769 (1) (2013) 9, http://dx.doi.org/10.1088/0004-637X/769/1/9.

[19] B. Edwards, Q. Changeat, A. Tsiaras, A. Allan, P. Behr, S.R. Hagey, M.D. Himes, S. Ma, K.G. Stassun, L. Thomas, A. Thompson, A. Boley, L. Booth, J. Bouwman, K. France, N. Lowson, A. Meech, C.L. Phillips, A.A. Vidotto, K.H. Yip, M. Bieger, A. Gressier, E. Janin, I.-G. Jiang, P. Leonardi, S. Sarkar, N. Skaf, J. Taylor, M. Yang, D. Ward-Thompson, Characterizing a world within the hot-neptune desert: Transit observations of LTT 9779 b with the hubble space telescope/WFC3, Astron. J. 166 (4) (2023) 158, http://dx.doi.org/10.3847/1538-3881/acea77.

[20] G.M. Szabó, S. Kálmán, The sub-Jupiter/Neptune desert of exoplanets: parameter dependent boundaries and implications on planet formation, Mon. Not. R. Astron. Soc.: Lett. (ISSN: 1745-3925) 485 (1) (2019) L116–L120, http://dx.doi.org/10.1093/mnrasl/slz036.

[21] C.M. Persson, I.Y. Georgieva, D. Gandolfi, L. Acuna, A. Aguichine, A. Muresan, E. Guenther, J. Livingston, K.A. Collins, F. Dai, M. Fridlund, E. Goffo, J.S. Jenkins, P. Kabáth, J. Korth, A.M. Levine, L.M. Serrano, J. Vines, O. Barragan, I. Carleo, K.D. Colon, W.D. Cochran, J.L. Christiansen, H.J. Deeg, M. Deleuil, D. Dragomir, M. Esposito, T. Gan, S. Grziwa, A.P. Hatzes, K. Hesse, K. Horne, J.M. Jenkins, J.F. Kielkopf, P. Klagyivik, K.W.F. Lam, D.W. Latham, R. Luque, J. Orell-Miquel, A. Mortier, O. Mousis, N. Narita, H.L.M. Osborne, E. Palle, R. Papini, G.R. Ricker, H. Schmerling, S. Seager, K.G. Stassun, V. Van Eylen, R. Vanderspek, G. Wang, J.N. Winn, B. Wohler, R. Zambelli, C. Ziegler, TOI-2196 b: Rare planet in the hot neptune desert transiting a G-type star, Astron. Astrophys. 666 (2022) A184, http://dx.doi.org/10.1051/0004-6361/202244118.

[22] B.J. Fulton, E.A. Petigura, A.W. Howard, H. Isaacson, G.W. Marcy, P.A. Cargile, L. Hebb, L.M. Weiss, J.A. Johnson, T.D. Morton, E. Sinukoff, I.J.M. Crossfield, L.A. Hirsch, The California-Kepler survey. III. A gap in the radius distribution of small planets, Astron. J. 154 (3) (2017) 109, http://dx.doi.org/10.3847/1538-3881/aa80eb.

[23] M. Zhang, H.A. Knutson, F. Dai, L. Wang, G.R. Ricker, R.P. Schwarz, C. Mann, K. Collins, Detection of atmospheric escape from four Young mini-neptunes, Astron. J. 165 (2) (2023) 62, http://dx.doi.org/10.3847/1538-3881/aca75b.

[24] J. Venturini, O.M. Guilera, J. Haldemann, M.P. Ronco, C. Mordasini, The nature of the radius valley - Hints from formation and evolution models, Astron. Astrophys. 643 (2020) L1, http://dx.doi.org/10.1051/0004-6361/202039141.

[25] A. Gupta, H.E. Schlichting, Signatures of the core-powered mass-loss mechanism in the exoplanet population: dependence on stellar properties and observational predictions, Mon. Not. R. Astron. Soc. (ISSN: 0035-8711) 493 (1) (2020) 792–806, http://dx.doi.org/10.1093/mnras/staa315.

[26] A. Izidoro, H.E. Schlichting, A. Isella, R. Dasgupta, C. Zimmermann, B. Bitsch, The exoplanet radius valley from gas-driven planet migration and breaking of resonant chains, Astrophys. J. Lett. 939 (2) (2022) L19, http://dx.doi.org/10.3847/2041-8213/ac990d.

[27] R. Burn, C. Mordasini, L. Mishra, J. Haldemann, J. Venturini, A. Emsenhuber, T. Henning, A radius valley between migrated steam worlds and evaporated rocky cores, Nat. Astron. (ISSN: 2397-3366) 8 (4) (2024) 463–471, http://dx.doi.org/10.1038/s41550-023-02183-7.

[28] R. Luque, E. Pallé, Density, not radius, separates rocky and water-rich small planets orbiting M dwarf stars, Science 377 (6611) (2022) 1211–1214, http://dx.doi.org/10.1126/science.abl7164, URL https://www.science.org/doi/abs/10.1126/science.abl7164.

[29] J.G. Rogers, J.E. Owen, Unveiling the planet population at birth, Mon. Not. R. Astron. Soc. (ISSN: 0035-8711) 503 (1) (2021) 1526–1542, http://dx.doi.org/10.1093/mnras/stab529.

[30] S.-M. Tsai, H. Innes, T. Lichtenberg, J. Taylor, M. Malik, K. Chubb, R. Pierrehumbert, Inferring shallow surfaces on sub-neptune exoplanets with JWST, Astrophys. J. Lett. 922 (2) (2021) L27, http://dx.doi.org/10.3847/2041-8213/ac399a.

[31] B. Benneke, P.-A. Roy, L.-P. Coulombe, M. Radica, C. Piaulet, E.-M. Ahrer, R. Pierrehumbert, J. Krissansen-Totton, H.E. Schlichting, R. Hu, J. Yang, D. Christie, D. Thorngren, E.D. Young, S. Pelletier, H.A. Knutson, Y. Miguel, T.M. Evans-Soma, C. Dorn, A. Gagnebin, J.J. Fortney, T. Komacek, R. MacDonald, E. Raul, R. Cloutier, L. Acuna, D. Lafrenière, C. Cadieux, R. Doyon, L. Welbanks, R. Allart, JWST reveals CH_4, CO_2, and h_2o in a metal-rich miscible atmosphere on a two-earth-radius exoplanet, 2024, URL https://arxiv.org/abs/2403.03325.

[32] E.M.-R. Kempton, H.A. Knutson, Transiting exoplanet atmospheres in the era of JWST, Rev. Miner. Geochem. (ISSN: 1529-6466) 90 (1) (2024) 411–464, http://dx.doi.org/10.2138/rmg.2024.90.12.

[33] S.H.C. Cabot, N. Madhusudhan, S. Constantinou, D. Valencia, J.M. Vos, T. Masseron, C.J. Cheverall, High-resolution spectroscopic reconnaissance of a temperate sub-neptune, Astrophys. J. Lett. 966 (1) (2024) L10, http://dx.doi.org/10.3847/2041-8213/ad3828.

[34] N.L. Wallack, N.E. Batalha, L. Alderson, N. Scarsdale, J.I.A. Redai, A. Aguichine, M.K. Alam, P. Gao, A. Wolfgang, N.M. Batalha, J. Kirk, M. López-Morales, S.E. Moran, J. Teske, H.R. Wakeford, N.F. Wogan, JWST COMPASS: A NIRSpec/G395H transmission spectrum of the sub-neptune TOI-836c, 2024, URL https://arxiv.org/abs/2404.01264.

[35] H. Gunell, R. Maggiolo, H. Nilsson, G. Stenberg Wieser, R. Slapak, J. Lindkvist, M. Hamrin, J. De Keyser, Why an intrinsic magnetic field does not protect a planet against atmospheric escape, Astron. Astrophys. 614 (2018) L3, http://dx.doi.org/10.1051/0004-6361/201832934.

[36] R. Ashtari, A. Sciola, J.D. Turner, K. Stevenson, Detecting magnetospheric radio emission from giant exoplanets, Astrophys. J. 939 (1) (2022) 24, http://dx.doi.org/10.3847/1538-4357/ac92f5.

[37] L. Ben-Jaffel, G.E. Ballester, A.G. Muñoz, P. Lavvas, D.K. Sing, J. Sanz-Forcada, O. Cohen, T. Kataria, G.W. Henry, L. Buchhave, T. Mikal-Evans, H.R. Wakeford, M. López-Morales, Signatures of strong magnetization and a metal-poor atmosphere for a neptune-sized exoplanet, Nat. Astron. (ISSN: 2397-3366) 6 (1) (2022) 141–153, http://dx.doi.org/10.1038/s41550-021-01505-x.

[38] J.D. Turner, P. Zarka, J.-M. Grießmeier, J. Lazio, B. Cecconi, J. Emilio Enriquez, J.N. Girard, R. Jayawardhana, L. Lamy, J.D. Nichols, I. de Pater, The search for radio emission from the exoplanetary systems 55 cancri, υ andromedae, and τ Boötis using LOFAR beam-formed observations, Astron. Astrophys. 645 (2021) A59, http://dx.doi.org/10.1051/0004-6361/201937201.

[39] J.O. Burns, R. MacDowall, S. Bale, G. Hallinan, N. Bassett, A. Hegedus, Low radio frequency observations from the moon enabled by NASA landed payload missions, Planet. Sci. J. 2 (2) (2021) 44, http://dx.doi.org/10.3847/PSJ/abdfc3.

[40] Y.A. Tanaka, T.K. Suzuki, S. ichiro Inutsuka, Atmospheric escape by magnetically driven wind from gaseous planets. ii. effects of magnetic diffusion, Astrophys. J. 809 (2) (2015) 125, http://dx.doi.org/10.1088/0004-637X/809/2/125.

[41] K. Fan, M. Fraenz, Y. Wei, J. Cui, Z. Rong, L. Chai, E. Dubinin, Deflection of global ion flow by the martian crustal magnetic fields, Astrophys. J. Lett. 898 (2) (2020) L54, http://dx.doi.org/10.3847/2041-8213/aba519.

[42] R. Lundin, H. Lammer, I. Ribas, Planetary magnetic fields and solar forcing: Implications for atmospheric evolution, Space Sci. Rev. (ISSN: 1572-9672) 129 (1) (2007) 245–278, http://dx.doi.org/10.1007/s11214-007-9176-4.

[43] I. Dandouras, Ion outflow and escape in the terrestrial magnetosphere: Cluster advances, J. Geophys. Res.: Space Phys. 126 (10) (2021) e2021JA029753.

[44] D. Ehrenreich, V. Bourrier, P.J. Wheatley, A.L. des Etangs, G. Hébrard, S. Udry, X. Bonfils, X. Delfosse, J.-M. Désert, D.K. Sing, A. Vidal-Madjar, A giant comet-like cloud of hydrogen escaping the warm Neptune-mass exoplanet GJ 436b, Nature (ISSN: 1476-4687) 522 (7557) (2015) 459–461, http://dx.doi.org/10.1038/nature14501.

[45] M.L. Khodachenko, I.F. Shaikhislamov, H. Lammer, A.G. Berezutsky, I.B. Miroshnichenko, M.S. Rumenskikh, K.G. Kislyakova, N.K. Dwivedi, Global 3D hydrodynamic modeling of in-transit lyα absorption of GJ 436b, Astrophys. J. 885 (1) (2019) 67, http://dx.doi.org/10.3847/1538-4357/ab46a4.

[46] G. Gronoff, P. Arras, S. Baraka, J.M. Bell, G. Cessateur, O. Cohen, S.M. Curry, J.J. Drake, M. Elrod, J. Erwin, K. Garcia-Sage, C. Garraffo, A. Glocer, N.G. Heavens, K. Lovato, R. Maggiolo, C.D. Parkinson, C. Simon Wedlund, D.R. Weimer, W.B. Moore, Atmospheric escape processes and planetary atmospheric evolution, J. Geophys. Res.: Space Phys. 125 (8) (2020) e2019JA027639, http://dx.doi.org/10.1029/2019JA027639, URL https://agupubs.onlinelibrary.wiley.com/doi/abs/10.1029/2019JA027639.

[47] J.E. Owen, Atmospheric escape and the evolution of close-in exoplanets, Annu. Rev. Earth Planet. Sci. (ISSN: 1545-4495) 47 (Volume 47, 2019) (2019) 67–90, http://dx.doi.org/10.1146/annurev-earth-053018-060246, URL https://www.annualreviews.org/content/journals/10.1146/annurev-earth-053018-060246.

[48] J.E. Owen, R.A. Murray-Clay, E. Schreyer, H.E. Schlichting, D. Ardila, A. Gupta, R.O.P. Loyd, E.L. Shkolnik, D.K. Sing, M.R. Swain, The fundamentals of Lyman α exoplanet transits, Mon. Not. R. Astron. Soc. (ISSN: 0035-8711) 518 (3) (2022) 4357–4371, http://dx.doi.org/10.1093/mnras/stac3414.

[49] L.A.G. dos Santos, Atmospheric Escape In Exoplanets: A Journey From Gas Giants To Earth Twins (Ph.D. thesis), UNIVERSITÉ DE GENÈVE, FACULTÉ DES SCIENCES, 2021, http://dx.doi.org/10.13097/archive-ouverte/unige:155240, URL https://archive-ouverte.unige.ch/unige:155240.

[50] D.J. Wilson, A. Youngblood, O. Toloza, J.J. Drake, K. France, C.S. Froning, B.T. Gänsicke, S. Redfield, B.E. Wood, Testing lyα emission-line reconstruction routines at multiple velocities in one system, Astrophys. J. 936 (2) (2022) 189, http://dx.doi.org/10.3847/1538-4357/ac87a8.

[51] A. Oklopčić, C.M. Hirata, A new window into escaping exoplanet atmospheres: 10830 Å line of helium, Astrophys. J. Lett. 855 (1) (2018) L11, http://dx.doi.org/10.3847/2041-8213/aaada9.

[52] A. Caldiroli, F. Haardt, E. Gallo, R. Spinelli, I. Malsky, E. Rauscher, Irradiation-driven escape of primordial planetary atmospheres. I. The ATES photoionization hydrodynamics code, Astron. Astrophys. 655 (2021) A30, http://dx.doi.org/10.1051/0004-6361/202141497.

[53] F. Biassoni, A. Caldiroli, E. Gallo, F. Haardt, R. Spinelli, F. Borsa, Self-consistent modeling of metastable helium exoplanet transits, Astron. Astrophys. 682 (2024) A115, http://dx.doi.org/10.1051/0004-6361/202347517.

[54] M. Salz, S. Czesla, P.C. Schneider, E. Nagel, J.H.M.M. Schmitt, L. Nortmann, F.J. Alonso-Floriano, M. López-Puertas, M. Lampón, F.F. Bauer, I.A.G. Snellen, E. Pallé, J.A. Caballero, F. Yan, G. Chen, J. Sanz-Forcada, P.J. Amado, A. Quirrenbach, I. Ribas, A. Reiners, V.J.S. Béjar, N. Casasayas-Barris, M. Cortés-Contreras, S. Dreizler, E.W. Guenther, T. Henning, S.V. Jeffers, A. Kaminski, M. Kürster, M. Lafarga, L.M. Lara, K. Molaverdikhani, D. Montes, J.C. Morales, A. Sánchez-López, W. Seifert, M.R. Zapatero Osorio, M. Zechmeister, Detection of HeI λ10830 Å absorption on HD 189733 b with CARMENES high-resolution transmission spectroscopy, Astron. Astrophys. 620 (2018) A97, http://dx.doi.org/10.1051/0004-6361/201833694.

[55] R. Allart, V. Bourrier, C. Lovis, D. Ehrenreich, J. Aceituno, A. Guijarro, F. Pepe, D.K. Sing, J.J. Spake, A. Wyttenbach, High-resolution confirmation of an extended helium atmosphere around WASP-107b, Astron. Astrophys. 623 (2019) A58, http://dx.doi.org/10.1051/0004-6361/201834917.

[56] S. Czesla, M. Lampón, J. Sanz-Forcada, A. García Muñoz, M. López-Puertas, L. Nortmann, D. Yan, E. Nagel, F. Yan, J.H.M.M. Schmitt, J. Aceituno, P.J. Amado, J.A. Caballero, N. Casasayas-Barris, T. Henning, S. Khalafinejad, K. Molaverdikhani, D. Montes, E. Pallé, A. Reiners, P.C. Schneider, I. Ribas, A. Quirrenbach, M.R. Zapatero Osorio, M. Zechmeister, Hα and HeI absorption in HAT-P-32 b observed with CARMENES - detection of roche lobe overflow and mass loss, Astron. Astrophys. 657 (2022) A6, http://dx.doi.org/10.1051/0004-6361/202039919.

[57] K. Paragas, S. Vissapragada, H.A. Knutson, A. Oklopčić, Y. Chachan, M. Greklek-McKeon, F. Dai, S. Tinyanont, G. Vasisht, Metastable helium reveals an extended atmosphere for the gas giant HAT-P-18b, Astrophys. J. Lett. 909 (1) (2021) L10, http://dx.doi.org/10.3847/2041-8213/abe706.

[58] T.T. Koskinen, R.V. Yelle, P. Lavvas, N.K. Lewis, Characterizing the thermosphere of hd209458b with uv transit observations, Astrophys. J. 723 (1) (2010) 116, http://dx.doi.org/10.1088/0004-637X/723/1/116.

[59] V. Bourrier, D. Ehrenreich, A. Lecavelier des Etangs, T. Louden, P.J. Wheatley, A. Wyttenbach, A. Vidal-Madjar, B. Lavie, F. Pepe, S. Udry, High-energy environment of super-earth 55 cancri e - I. Far-UV chromospheric variability as a possible tracer of planet-induced coronal rain, Astron. Astrophys. 615 (2018) A117, http://dx.doi.org/10.1051/0004-6361/201832700.

[60] L. Fossati, K. France, T. Koskinen, I.G. Juvan, C.A. Haswell, M. Lendl, Far-UV spectroscopy of the planet-hosting star WASP-13: high-energy irradiance, distance, age, planetary mass-loss rate, and circumstellar environment*, Astrophys. J. 815 (2) (2015) 118, http://dx.doi.org/10.1088/0004-637X/815/2/118.

[61] A.A. Vidotto, M. Jardine, C. Helling, Prospects for detection of exoplanet magnetic fields through bow-shock observations during transits, Mon. Not. R. Astron. Soc.: Lett. (ISSN: 1745-3925) 411 (1) (2011) L46–L50, http://dx.doi.org/10.1111/j.1745-3933.2010.00991.x.

[62] J. Llama, A.A. Vidotto, M. Jardine, K. Wood, R. Fares, T.I. Gombosi, Exoplanet transit variability: bow shocks and winds around HD 189733b, Mon. Not. R. Astron. Soc. (ISSN: 0035-8711) 436 (3) (2013) 2179–2187, http://dx.doi.org/10.1093/mnras/stt1725.

[63] J. Llama, K. Wood, M. Jardine, A.A. Vidotto, C. Helling, L. Fossati, C.A. Haswell, The shocking transit of WASP-12b: modelling the observed early ingress in the near-ultraviolet, Mon. Not. R. Astron. Soc.: Lett. (ISSN: 1745-3925) 416 (1) (2011) L41–L44, http://dx.doi.org/10.1111/j.1745-3933.2011.01093.x.

[64] D. Lai, C. Helling, E.P.J. van den Heuvel, Mass transfer, transiting stream, and magnetopause in close-in exoplanetary systems with applications to WASP-12, Astrophys. J. 721 (2) (2010) 923, http://dx.doi.org/10.1088/0004-637X/721/2/923.

[65] A.A. Vidotto, M. Jardine, C. Helling, Early uv ingress iN WASP-12b: measuring planetary magnetic fields, Astrophys. J. Lett. 722 (2) (2010) L168, http://dx.doi.org/10.1088/2041-8205/722/2/L168.

[66] A.G. Jensen, P.W. Cauley, S. Redfield, W.D. Cochran, M. Endl, Hydrogen and sodium absorption in the optical transmission spectrum of WASP-12b, Astron. J. 156 (4) (2018) 154, http://dx.doi.org/10.3847/1538-3881/aadca7.

[67] S. Czesla, M. Lampón, D. Cont, F. Lesjak, J. Orell-Miquel, J. Sanz-Forcada, E. Nagel, L. Nortmann, K. Molaverdikhani, M. López-Puertas, F. Yan, A. Quirrenbach, J.A. Caballero, E. Pallé, J. Aceituno, P.J. Amado, T. Henning, S. Khalafinejad, D. Montes, A. Reiners, I. Ribas, A. Schweitzer, The elusive atmosphere of WASP–12 b - high-resolution transmission spectroscopy with CARMENES, Astron. Astrophys. 683 (2024) A67, http://dx.doi.org/10.1051/0004-6361/202348107.

[68] K. Herbst, L.R. Baalmann, A. Bykov, N.E. Engelbrecht, S.E.S. Ferreira, V.V. Izmodenov, S.D. Korolkov, K.P. Levenfish, J.L. Linsky, D.M.-A. Meyer, K. Scherer, R.D.T. Strauss, Astrospheres of planet-hosting cool stars and beyond - when modeling meets observations, Space Sci. Rev. (ISSN: 1572-9672) 218 (4) (2022) 29, http://dx.doi.org/10.1007/s11214-022-00894-3.

[69] D. Grether, C.H. Lineweaver, How dry is the brown dwarf desert? Quantifying the relative number of planets, brown dwarfs, and stellar companions around nearby sun-like stars, Astrophys. J. 640 (2) (2006) 1051, http://dx.doi.org/10.1086/500161.

[70] D.R. Anderson, A.C. Cameron, C. Hellier, M. Lendl, P.F.L. Maxted, D. Pollacco, D. Queloz, B. Smalley, A.M.S. Smith, I. Todd, A.H.M.J. Triaud, R.G. West, S.C.C. Barros, B. Enoch, M. Gillon, T.A. Lister, F. Pepe, D. Ségransan, R.A. Street, S. Udry, WASP-30b: A 61 mjup BROWN dwarf transiting a v=12, F8 STAR, Astrophys. J. Lett. 726 (2) (2010) L19, http://dx.doi.org/10.1088/2041-8205/726/2/L19.

[71] F. Bouchy, M. Deleuil, T. Guillot, S. Aigrain, L. Carone, W.D. Cochran, J.M. Almenara, R. Alonso, M. Auvergne, A. Baglin, P. Barge, A.S. Bonomo, P. Bordé, S. Csizmadia, K. De Bondt, H.J. Deeg, R.F. Díaz, R. Dvorak, M. Endl, A. Erikson, S. Ferraz-Mello, M. Fridlund, D. Gandolfi, J.C. Gazzano, N. Gibson, M. Gillon, E. Guenther, A. Hatzes, M. Havel, G. Hébrard, L. Jorda, A. Léger, C. Lovis, A. Llebaria, H. Lammer, P.J. MacQueen, T. Mazeh, C. Moutou, A. Ofir, M. Ollivier, H. Parviainen, M. Pätzold, D. Queloz, H. Rauer, D. Rouan, A. Santerne, J. Schneider, B. Tingley, G. Wuchterl, Transiting exoplanets from the CoRoT space mission - XV. CoRoT-15b: a brown-dwarf transiting companion, Astron. Astrophys. 525 (2011) A68, http://dx.doi.org/10.1051/0004-6361/201015276.

[72] J. Šubjak, R. Sharma, T.W. Carmichael, M.C. Johnson, E.J. Gonzales, E. Matthews, H.M.J. Boffin, R. Brahm, P. Chaturvedi, A. Chakraborty, D.R. Ciardi, K.A. Collins, M. Esposito, M. Fridlund, T. Gan, D. Gandolfi, R.A. García, E. Guenther, A. Hatzes, D.W. Latham, S. Mathis, S. Mathur, C.M. Persson, H.M. Relles, J.E. Schlieder, T. Barclay, C.D. Dressing, I. Crossfield, A.W. Howard, F. Rodler, G. Zhou, S.N. Quinn, G.A. Esquerdo, M.L. Calkins, P. Berlind, K.G. Stassun, M. Blažek, M. Skarka, M. Špoková, J. Žák, S. Albrecht, R.A. Sobrino, P. Beck, J. Cabrera, I. Carleo, W.D. Cochran, S. Csizmadia, F. Dai, H.J. Deeg, J.P. de Leon, P. Eigmüller, M. Endl, A. Erikson, A. Fukui, I. Georgieva, L. González-Cuesta, S. Grziwa, D. Hidalgo, T. Hirano, M. Hjorth, E. Knudstrup, J. Korth, K.W.F. Lam, J.H. Livingston, M.N. Lund, R. Luque, P.M. Rodríguez, F. Murgas, N. Narita, D. Nespral, P. Niraula, G. Nowak, E. Pallé, M. Pätzold, J. Prieto-Arranz, H. Rauer, S. Redfield, I. Ribas, A.M.S. Smith, V.V. Eylen, P. Kabáth, TOI-503: The first known brown-dwarf am-star binary from the TESS mission, Astron. J. 159 (4) (2020) 151, http://dx.doi.org/10.3847/1538-3881/ab7245.

[73] P. Benni, A.Y. Burdanov, V.V. Krushinsky, A. Bonfanti, G. Hébrard, J.M. Almenara, S. Dalal, O.D.S. Demangeon, M. Tsantaki, J. Pepper, K.G. Stassun, A. Vanderburg, A. Belinski, F. Kashaev, K. Barkaoui, T. Kim, W. Kang, K. Antonyuk, V.V. Dyachenko, D.A. Rastegaev, A. Beskakotov, A.A. Mitrofanova, F.J. Pozuelos, E.D. Kuznetsov, A. Popov, F. Kiefer, P.A. Wilson, G. Ricker, R. Vanderspek, D.W. Latham, S. Seager, J.M. Jenkins, E. Sokov, I. Sokova, A. Marchini, R. Papini, F. Salvaggio, M. Banfi, O. Baştürk, S. Torun, S. Yalçınkaya, K. Ivanov, G. Valyavin, E. Jehin, M. Gillon, E. Pakštienė, V.-P. Hentunen, S. Shadick, M. Bretton, A. Wünsche, J. Garlitz, Y. Jongen, D. Molina, E. Girardin, F. Grau Horta, R. Naves, Z. Benkhaldoun, M.D. Joner, M. Spencer, A. Bieryla, D.J. Stevens, E.L.N. Jensen, K.A. Collins, D. Charbonneau, E.V. Quintana, S.E. Mullally, C.E. Henze, Discovery of a young low-mass brown dwarf transiting a fast-rotating F-type star by the galactic plane exoplanet (GPX) survey, Mon. Not. R. Astron. Soc. (ISSN: 0035-8711) 505 (4) (2021) 4956–4967, http://dx.doi.org/10.1093/mnras/stab1567.

[74] E. Artigau, G. Hébrard, C. Cadieux, T. Vandal, N.J. Cook, R. Doyon, J. Gagné, C. Moutou, E. Martioli, A. Frasca, F. Jahandar, D. Lafrenière, L. Malo, J.-F. Donati, P. Cortés-Zuleta, I. Boisse, X. Delfosse, A. Carmona, P. Fouqué, J. Morin, J. Rowe, G. Marino, R. Papini, D.R. Ciardi, M.B. Lund, J.H.C. Martins, S. Pelletier, L. Arnold, F. Bouchy, T. Forveille, N.C. Santos, X. Bonfils, P. Figueira, M. Fausnaugh, G. Ricker, D.W. Latham, S. Seager, J.N. Winn, J.M. Jenkins, E.B. Ting, G. Torres, J.G. da Silva, TOI–1278 B: Spirou unveils a rare brown dwarf companion in close-in orbit around an M dwarf, Astron. J. 162 (4) (2021) 144, http://dx.doi.org/10.3847/1538-3881/ac096d.

[75] T.W. Carmichael, Improved radius determinations for the transiting brown dwarf population in the era of gaia and TESS, Mon. Not. R. Astron. Soc. (ISSN: 0035-8711) 519 (4) (2022) 5177–5190, http://dx.doi.org/10.1093/mnras/stac3720.

[76] M. Montalto, G. Piotto, P.M. Marrese, V. Nascimbeni, L. Prisinzano, V. Granata, S. Marinoni, S. Desidera, S. Ortolani, C. Aerts, E. Alei, G. Altavilla, S. Benatti, A. Börner, J. Cabrera, R. Claudi, M. Deleuil, M. Fabrizio, L. Gizon, M.J. Goupil, A.M. Heras, D. Magrin, L. Malavolta, J.M. Mas-Hesse, I. Pagano, C. Paproth, M. Pertenais, D. Pollacco, R. Ragazzoni, G. Ramsay, H. Rauer, S. Udry, The all-sky PLATO input catalogue, Astron. Astrophys. 653 (2021) A98, http://dx.doi.org/10.1051/0004-6361/202140717.

[77] H. Rauer, C. Aerts, J. Cabrera, PLATO Team, The PLATO mission, Astron. Nachr. 337 (8–9) (2016) 961–963, http://dx.doi.org/10.1002/asna.201612408, URL https://onlinelibrary.wiley.com/doi/abs/10.1002/asna.201612408.

[78] H. Rauer, M. Fridlund, PLATO 2.0 satellite, in: M. Gargaud, W.M. Irvine, R. Amils, P. Claeys, H.J. Cleaves, M. Gerin, D. Rouan, T. Spohn, S. Tirard, M. Viso (Eds.), Encyclopedia of Astrobiology, Springer Berlin Heidelberg, Berlin, Heidelberg, ISBN: 978-3-662-65093-6, 2023, pp. 2405–2407, http://dx.doi.org/10.1007/978-3-662-65093-6_1760.

[79] J.N. Bahcall, L. Spitzer, The space telescope, Sci. Am. 247 (1) (1982) 40–51, ISSN: (00368733, 19467087), URL http://www.jstor.org/stable/24966634.

[80] E. Chaisson, R. Villard, The science mission of the hubble space telescope, Vistas Astron. (ISSN: 0083-6656) 33 (1990) 105–141, http://dx.doi.org/10.1016/0083-6656(90)90018-4, URL https://www.sciencedirect.com/science/article/pii/0083665690900184.

[81] J.P. Gardner, J.C. Mather, M. Clampin, R. Doyon, M.A. Greenhouse, H.B. Hammel, J.B. Hutchings, P. Jakobsen, S.J. Lilly, K.S. Long, J.I. Lunine, M.J. Mccaughrean, M. Mountain, J. Nella, G.H. Rieke, M.J. Rieke, H.-W. Rix, E.P. Smith, G. Sonneborn, M. Stiavelli, H.S. Stockman, R.A. Windhorst, G.S. Wright, The james webb space telescope, Space Sci. Rev. (ISSN: 1572-9672) 123 (4) (2006) 485–606, http://dx.doi.org/10.1007/s11214-006-8315-7.

[82] G. Tinetti, P. Drossart, P. Eccleston, P. Hartogh, A. Heske, J. Leconte, G. Micela, M. Ollivier, G. Pilbratt, L. Puig, D. Turrini, B. Vandenbussche, P. Wolkenberg, E. Pascale, J.-P. Beaulieu, M. Güdel, M. Min, M. Rataj, T. Ray, I. Ribas, J. Barstow, N. Bowles, A. Coustenis, V.C. du Foresto, L. Decin, T. Encrenaz, F. Forget, M. Friswell, M. Griffin, P.O. Lagage, P. Malaguti, A. Moneti, J.C. Morales, E. Pace, M. Rocchetto, S. Sarkar, F. Selsis, W. Taylor, J. Tennyson, O. Venot, I.P. Waldmann, G. Wright, T. Zingales, M.R. Zapatero-Osorio, The science of ARIEL (atmospheric remote-sensing infrared exoplanet large-survey), in: H.A. MacEwen, G.G. Fazio, M. Lystrup, N. Batalha, N. Siegler, E.C. Tong (Eds.), in: Space Telescopes and Instrumentation 2016: Optical, Infrared, and Millimeter Wave, vol. 9904, International Society for Optics and Photonics, SPIE, 2016, p. 99041X, http://dx.doi.org/10.1117/12.2232370.

[83] P. Eccleston, G. Tinetti, J.-P. Beaulieu, M. Güdel, P. Hartogh, G. Micela, M. Min, M. Rataj, T. Ray, I. Ribas, B. Vandenbussche, J.-L. Augueres, G. Bishop, V.D. Deppo, M. Focardi, T. Hunt, G. Malaguti, K. Middleton, G. Morgante, M. Ollivier, E. Pace, E. Pascale, W. Taylor, An integrated payload design for the atmospheric remote-sensing infrared exoplanet large-survey (ARIEL), in: H.A. MacEwen, G.G. Fazio, M. Lystrup, N. Batalha, N. Siegler, E.C. Tong (Eds.), in: Space Telescopes and Instrumentation 2016: Optical, Infrared, and Millimeter Wave, vol. 9904, International Society for Optics and Photonics, SPIE, 2016, 990433, http://dx.doi.org/10.1117/12.2232878.

[84] S.M. Birkmann, P. Ferruit, G. Giardino, L.D. Nielsen, A. García Muñoz, S. Kendrew, B.J. Rauscher, T.L. Beck, C. Keyes, J.A. Valenti, P. Jakobsen, B. Dorner, C. Alves de Oliveira, S. Arribas, T. Böker, A.J. Bunker, S. Charlot, G. de Marchi, N. Kumari, M. López-Caniego, N. Lützgendorf, R. Maiolino, E. Manjavacas, A. Marston, S.H. Moseley, N. Prizkal, C. Proffitt, T. Rawle, H.-W. Rix, M. te Plate, E. Sabbi, M. Sirianni, C.J. Willott, P. Zeidler, The near-infrared spectrograph (NIRSpec) on the james webb space telescope - IV. Capabilities and predicted performance for exoplanet characterization, Astron. Astrophys. 661 (2022) A83, http://dx.doi.org/10.1051/0004-6361/202142592.

[85] European Space Agency, ARIEL payload, 2023, Online, URL https://sci.esa.int/web/ariel/-/59801-payload. (Accessed 19 July 2023).

[86] L. Ben-Jaffel, Exoplanet HD 209458b: Inflated hydrogen atmosphere but no sign of evaporation, Astrophys. J. 671 (1) (2007) L61, http://dx.doi.org/10.1086/524706.

[87] L.J. Tacconi, C.S. Arridge, A. Buonanno, M. Cruise, O. Grasset, A. Helmi, L. Iess, E. Komatsu, J. Leconte, J. Leenaarts, J. Martín-Pintado, R. Nakamura, D. Watson, Voyage 2050 - final recommendations from the voyage 2050 senior committee, 2021, Online, URL https://www.cosmos.esa.int/documents/1866264/1866292/Voyage2050-Senior-Committee-report-public.pdf/e2b2631e-5348-5d2d-60c1-437225981b6b?t=1623427287109. (Accessed 31 March 2025).

[88] K. Jahnke, O. Krause, H.-W. Rix, F. Courbin, A. Fontana, C. Heymans, N. Martin, P. Oesch, A. Taylor, B.S. Gaudi, A. Kiessling, B. Mennesson, S. Seager, D. Stern, K. Warfield, The need for a multi-purpose, optical–NIR space facility after HST and JWST, Exp. Astron. (ISSN: 1572-9508) 51 (3) (2021) 765–782, http://dx.doi.org/10.1007/s10686-021-09732-w.

[89] H. Linz, H. Beuther, M. Gerin, J.R. Goicoechea, F. Helmich, O. Krause, Y. Liu, S. Molinari, V. Ossenkopf-Okada, J. Pineda, M. Sauvage, E. Schinnerer, F. van der Tak, M. Wiedner, Bringing high spatial resolution to the far-infrared – a giant leap for astrophysics, 2020, URL https://arxiv.org/abs/2002.06693.

[90] A. Zanella, C. Zanoni, F. Arrigoni-Battaia, A. Rubin, A. Pala, C. Peroux, R. Augustin, C. Circosta, E. Emsellem, E. George, D. Milakovic, R. van der Burg, T. Kupfer, Unveiling the faint ultraviolet universe, 2021, URL https://arxiv.org/abs/1910.01194.

[91] L. Rossi, J. Berzosa-Molina, J.-M. Desert, L. Fossati, A.G. Muñoz, C. Haswell, P. Kabath, K. Kislyakova, D. Stam, A. Vidotto, Spectropolarimetry as a tool for understanding the diversity of planetary atmospheres, Exp. Astron. (ISSN: 1572-9508) 54 (2) (2022) 1187–1196, http://dx.doi.org/10.1007/s10686-021-09813-w.

[92] C. Neiner, J. Morin, J.C. Bouret, L. Fossati, Stellar physics with high-resolution UV spectropolarimetry, 2019, URL https://arxiv.org/abs/1903.06509.

[93] V. Lebouteiller, C.G.H. Yan, P. Richter, B. Godard, E.B. Jenkins, D. Welty, N. Lehner, P. Guillard, J. Roman-Duval, E. Roueff, F. Leone, D. Kunth, J.C. Howk, P. Boissé, F. Boulanger, E. Bron, B. James, J.L. Bourlot, F.L. Petit, M. Pieri, V. Valdivia, ESA voyage 2050 white paper: A complete census of the gas phases in and around galaxies, far-UV spectropolarimetry as a prime tool for understanding galaxy evolution and star formation, 2019, URL https://arxiv.org/abs/1909.03056.

[94] R. Cilley, G.W. King, L. Corrales, Detecting exoplanet transits with the next generation of X-Ray telescopes, Astron. J. 168 (4) (2024) 177, http://dx.doi.org/10.3847/1538-3881/ad6d60.

[95] M. Cruise, M. Guainazzi, J. Aird, F.J. Carrera, E. Costantini, L. Corrales, T. Dauser, D. Eckert, F. Gastaldello, H. Matsumoto, R. Osten, P.-O. Petrucci, D. Porquet, G.W. Pratt, N. Rea, T.H. Reiprich, A. Simionescu, D. Spiga, E. Troja, The NewAthena mission concept in the context of the next decade of X-ray astronomy, Nat. Astron. (ISSN: 2397-3366) 9 (1) (2025) 36–44, http://dx.doi.org/10.1038/s41550-024-02416-3.

[96] E.V. Quintana, J.L. Dotson, K.D. Colón, T. Barclay, P. Supsinskas, J. Karburn, D. Apai, C. Hedges, B.V. Rackham, J.F. Rowe, N.H. Allen, P. Bonney, S. Cano, J.L. Christiansen, D. Ciardi, N. Espinoza, T.O. Foote, E.A. Gilbert, T.P. Greene, K. Hoffman, B.J. Hord, A. Iyer, A. Kesseli, V.B. Kostov, N.K. Lewis, S.E. Logsdon, A.W. Mann, M. Mansfield, J. Mason, B.M. Morris, G. Mosby, S.E. Mullally, E.R. Newton, F. Nguyen, J.E. Schlieder, K.B. Stevenson, L.S. Wiser, A. Youngblood, R.T. Zellem, The pandora SmallSat: multiwavelength characterization of exoplanets and their host stars, in: L.E. Coyle, S. Matsuura, M.D. Perrin (Eds.), in: Space Telescopes and Instrumentation 2024: Optical, Infrared, and Millimeter Wave, vol. 13092, SPIE, International Society for Optics and Photonics, 2024, 1309214, http://dx.doi.org/10.1117/12.3020633.

[97] M. Balakrishnan, R. Bowens, F. Cruz Aguirre, K. Hughes, R. Jayaraman, E. Kuhn, E. Louden, D.R. Louie, K. McBride, C. McGrath, J. Payne, T. Presser, J.S. Reding, E. Rickman, R. Scrandis, T. Symons, L. Wiser, K. Jahoda, T. Kataria, A. Nash, T. X, MAUVE: An ultraviolet astrophysics probe mission concept, Publ. Astron. Soc. Pac. 136 (10) (2024) 105002, http://dx.doi.org/10.1088/1538-3873/ad77f3.

[98] J.M. O'Meara, M. Ansdell, J. Crooke, J. Pepper, L. Feinberg, A. Roberge, J. Ziemer, B. Mennesson, C. Dressing, The habitable worlds observatory science view: status, plans, and opportunities, in: L.E. Coyle, S. Matsuura, M.D. Perrin (Eds.), in: Space Telescopes and Instrumentation 2024: Optical, Infrared, and Millimeter Wave, vol. 13092, International Society for Optics and Photonics, SPIE, 2024, p. 130921M, http://dx.doi.org/10.1117/12.3019387.

[99] The LUVOIR Team, The LUVOIR mission concept study final report, 2019, URL https://arxiv.org/abs/1912.06219.

[100] E. Palle, K. Biazzo, E. Bolmont, P. Molliere, K. Poppenhaeger, J. Birkby, M. Brogi, G. Chauvin, A. Chiavassa, J. Hoeijmakers, E. Lellouch, C. Lovis, R. Maiolino, L. Nortmann, H. Parviainen, L. Pino, M. Turbet, J. Wender, S. Albrecht, S. Antoniucci, S.C. Barros, A. Beaudoin, B. Benneke, I. Boisse, A.S. Bonomo, F. Borsa, A. Brandeker, W. Brandner, L.A. Buchhave, A.-L. Cheffot, R. Deborde, F. Debras, R. Doyon, P. Di Marcantonio, P. Giacobbe, J.I.G. Hernandez, R. Helled, L. Kreidberg, P. Machado, J. Maldonado, A. Marconi, B.L.C. Martins, A. Miceli, C. Mordasini, M. N'Diaye, A. Niedzielski, B. Nisini, L. Origlia, C. Peroux, A.G.M. Pietrow, E. Pinna, E. Rauscher, S. Reffert, P. Rousselot, N. Sanna, A. Simonnin, A.S. Mascareno, A. Zanutta, M. Zechmeister, Ground-breaking exoplanet science with the ANDES spectrograph at the ELT, 2023, URL https://arxiv.org/abs/2311.17075.

[101] M. Kasper, J.-L. Beuzit, C. Verinaud, P. Baudoz, A. Boccaletti, R. Gratton, C. Keller, F. Kerber, H. Schmid, N. Thatte, L. Venema, N. Yaitskova, EPICS, the exoplanet imager for the E-ELT, 2010, p. 02009, http://dx.doi.org/10.1051/ao4elt/201002009.

[102] G.F. Benedict, E. Nelan, D. Story, B. McArthur, A.L. Whipple, W.H. Jefferys, W. van Altena, P.D. Hemenway, P.J. Shelus, O.G. Franz, A. Bradley, L.W. Fredrick, R.L. Duncombe, Astrometric performance characteristics of the hubble space telescope fine guidance sensors, Publ. Astron. Soc. Pac. 104 (680) (1992) 958, http://dx.doi.org/10.1086/133081.

[103] E.P. Nelan, O.L. Lupie, B. McArthur, G.F. Benedict, O.G. Franz, L.H. Wasserman, L. Abramowicz-Reed, R.B. Makidon, L. Nagel, Fine guidance sensors aboard the hubble space te lescope: the scientific capabilities of these interferometers, in: R.D. Reasenberg (Ed.), in: Astronomical Interferometry, vol. 3350, International Society for Optics and Photonics, SPIE, 1998, pp. 237–247, http://dx.doi.org/10.1117/12.317121.

[104] G.S. Nurre, S.J. Anhouse, S.N. Gullapalli, Hubble space telescope fine guidance sensor control system, in: S. Gowrinathan (Ed.), in: Acquisition, Tracking, and Pointing III, vol. 1111, International Society for Optics and Photonics, SPIE, 1989, pp. 327–343, http://dx.doi.org/10.1117/12.977993.

[105] J.A.B. Termini, K. Hoadley, C. DeRoo, C. Fasano, E. Hamden, J. Li, Determining ideal grating parameters for UV blazed gratings, in: J.-W.A. den Herder, S. Nikzad, K. Nakazawa (Eds.), in: Space Telescopes and Instrumentation 2022: Ultraviolet To Gamma Ray, vol. 12181, International Society for Optics and Photonics, SPIE, 2022, p. 121812Q, http://dx.doi.org/10.1117/12.2628739.

[106] B. Guldimann, A. Deep, R. Vink, Overview on grating developments at ESA, CEAS Space J. (ISSN: 18682510) 7 (2015) 433–451, http://dx.doi.org/10.1007/S12567-015-0095-Z/TABLES/5, URL https://link.springer.com/article/10.1007/s12567-015-0095-z.

[107] S. Zha, D. Li, Q. Wen, Y. Zhou, H. Zhang, Design and fabrication of silicon-blazed gratings for near-infrared scanning grating micromirror, Micromachines (ISSN: 2072666X) 13 (2022) http://dx.doi.org/10.3390/MI13071000.

[108] J.J. Hennessy, K. Balasubramanian, C.S. Moore, A.D. Jewell, S. Nikzad, K.C. France, M.A. Quijada, Performance and prospects of far ultraviolet aluminum mirrors protected by atomic layer deposition, J. Astron. Telesc. Instrum. Syst. 2 (4) (2016) 041206, http://dx.doi.org/10.1117/1.JATIS.2.4.041206.

[109] Y. Ozaki, Y. Saito, S. Kawata, Introduction to FUV and DUV spectroscopy, in: Y. Ozaki, S. Kawata (Eds.), Far- and Deep-Ultraviolet Spectroscopy, Springer Japan, Tokyo, ISBN: 978-4-431-55549-0, 2015, pp. 1–16, http://dx.doi.org/10.1007/978-4-431-55549-0_1.

[110] M.P. Ulmer, Future UV detectors for space applications, Opt. Sens. II (ISSN: 0277786X) 6189 (2006) 61890W, http://dx.doi.org/10.1117/12.668238,

[111] L.J. Paxton, R.K. Schaefer, Y. Zhang, H. Kil, Far ultraviolet instrument technology, J. Geophys. Res.: Space Phys. 122 (2) (2017) 2706–2733, http://dx.doi.org/10.1002/2016JA023578, URL https://agupubs.onlinelibrary.wiley.com/doi/abs/10.1002/2016JA023578.

[112] S. Nikzad, M. Hoenk, A.D. Jewell, J.J. Hennessy, A.G. Carver, T.J. Jones, T.M. Goodsall, E.T. Hamden, P. Suvarna, J. Bulmer, F. Shahedipour-Sandvik, E. Charbon, P. Padmanabhan, B. Hancock, L.D. Bell, Single photon counting UV solar-blind detectors using silicon and III-nitride materials, Sensors (ISSN: 1424-8220) 16 (6) (2016) http://dx.doi.org/10.3390/s16060927, URL https://www.mdpi.com/1424-8220/16/6/927.

[113] S. Nikzad, M.E. Hoenk, F. Greer, B. Jacquot, S. Monacos, T.J. Jones, J. Blacksberg, E. Hamden, D. Schiminovich, C. Martin, P. Morrissey, Delta-doped electron-multiplied CCD with absolute quantum efficiency over 50% in the near to far ultraviolet range for single photon counting applications, Appl. Opt. 51 (3) (2012) 365–369, http://dx.doi.org/10.1364/AO.51.000365, URL https://opg.optica.org/ao/abstract.cfm?URI=ao-51-3-365.

[114] O. Gravrand, J. Rothman, P. Castelein, C. Cervera, N. Baier, C. Lobre, E.D. Borniol, J.P. Zanatta, O. Boulade, V. Moreau, B. Fieque, P. Chorier, Latest achievements on MCT IR detectors for space and science imaging, in: B. rn F. Andresen, G.F. Fulop, C.M. Hanson, P.R. Norton (Eds.), in: Infrared Technology and Applications XLII, vol. 9819, International Society for Optics and Photonics, SPIE, 2016, p. 98191W, http://dx.doi.org/10.1117/12.2228456.

[115] Chroma Technology Corp, 27003 H-alpha 8nm bandpass, 2025, Online, URL https://www.chroma.com/products/parts/27003-h-alpha-8nm-bandpass#legend-selector1. (Accessed 11 March 2025).

[116] J.D. Turner, K.A. Pearson, L.I. Biddle, B.M. Smart, R.T. Zellem, J.K. Teske, K.K. Hardegree-Ullman, C.C. Griffith, R.M. Leiter, I.T. Cates, M.N. Nieberding, C.-T.W. Smith, R.M. Thompson, R. Hofmann, M.P. Berube, C.H. Nguyen, L.C. Small, B.C. Guvenen, L. Richardson, A. McGraw, B. Raphael, B.E. Crawford, A.N. Robertson, R. Tombleson, T.M. Carleton, A.P. Towner, A.M. Walker-LaFollette, J.R. Hume, Z.T. Watson, C.K. Jones, M.J. Lichtenberger, S.R. Hoglund, K.L. Cook, C.A. Crossen, C.R. Jorgensen, J.M. Romine, A.R. Thompson, C.F. Villegas, A.A. Wilson, B. Sanford, J.M. Taylor, T.N. Henz, Ground-based near-UV observations of 15 transiting exoplanets: constraints on their atmospheres and no evidence for asymmetrical transits, Mon. Not. R. Astron. Soc. (ISSN: 0035-8711) 459 (1) (2016) 789–819, http://dx.doi.org/10.1093/mnras/stw574.

[117] S. Kameda, S. Ikezawa, M. Sato, M. Kuwabara, N. Osada, G. Murakami, K. Yoshioka, I. Yoshikawa, M. Taguchi, R. Funase, S. Sugita, Y. Miyoshi, M. Fujimoto, Ecliptic north-south symmetry of hydrogen geocorona, Geophys. Res. Lett. 44 (23) (2017) 11,706–11,712, http://dx.doi.org/10.1002/2017GL075915, URL https://agupubs.onlinelibrary.wiley.com/doi/abs/10.1002/2017GL075915.

[118] SRE-PA and D-TEC staff, Margin philosophy for science assessment studies, 2012, ESA Technical Note SRE-PA/2011.097, Issue 1, Revision 3, URL https://sci.esa.int/documents/34375/36249/1567260131067-Margin_philosophy_for_science_assessment_studies_1.3.pdf.

[119] Ariane Group, 20N monopropellant hydrazine thruster, 2023, Online, URL https://www.space-propulsion.com/spacecraft-propulsion/hydrazine-thrusters/20n-hydrazine-thruster.html. (Accessed 13 December 2023).

[120] Ariane Group, Surface tension propellant tank OST 33/0, 2023, Online, URL https://www.space-propulsion.com/spacecraft-propulsion/hydrazine-tanks/index.html#176. (Accessed 13 December 2023).

[121] U. Swami, N. Kumbhakarna, A. Chowdhury, Green hypergolic ionic liquids: Future rocket propellants, J. Ion. Liq. (ISSN: 2772-4220) 2 (2) (2022) 100039, http://dx.doi.org/10.1016/j.jil.2022.100039, URL https://www.sciencedirect.com/science/article/pii/S2772422022000234.

[122] ECAPS, HPGP thrusters, 2023, Online, URL https://www.ecaps.se/rocket-engines. (Accessed 13 December 2023).

[123] sodern Ariane Group, Hydra - highly resilient modular star tracker, 2023, Online, URL https://sodern.com/wp-content/uploads/2023/12/2023-12-Hydra-family.pdf. (Accessed 13 December 2023).

[124] Airbus Space and Defence, Astrix inertial measurement IRU series - astrix 200, 2023, Online, URL https://www.airbus.com/sites/g/files/jlcbta136/files/2022-02/ScE-AVIONICS-ASTRIX200v3_2022.pdf. (Accessed 13 December 2023).

[125] Lens Research and Development, Bison64-ET fm, 2023, Online, URL https://lens-rnd.com/products/-bison64-et-fm. (Accessed 13 December 2023).

[126] Airbus Space and Defence, Platform electronics - ICDE NG, 2023, Online, URL https://mediaassets.airbus.com/pm_38_552_552292-93cxf94est.pdf. (Accessed 13 December 2023).

[127] Bradfort, W18E RWA, 2023, Online, URL https://static1.squarespace.com/static/603ed12be884730013401d7a/t/6054f630baf06f76bbabe02a/1616180789682/be_datasheet_rwu_2019dec.pdf. (Accessed 13 December 2023).

[128] Ariane Group, 1N monopropellant hydrazine thruster, 2023, Online, URL https://www.space-propulsion.com/spacecraft-propulsion/hydrazine-thrusters/1n-hydrazine-thruster.html. (Accessed 13 December 2023).

[129] Airbus Space and Defence, Platform electronics - oscar, 2023, Online, URL https://www.airbus.com/sites/g/files/jlcbta136/files/2022-05/datasheet-oscar-2022v2.pdf. (Accessed 13 December 2023).

[130] Airbus Space and Defence, Nemo2 2040, 2023, Online, URL https://www.airbus.com/sites/g/files/jlcbta136/files/2021-11/datasheet-datahandling-nemo2-2021.04v1.4.pdf. (Accessed 13 December 2023).

[131] Airbus Space and Defence, Mechanism products & engineering Germany - exploration X-XAS, 2023, Online, URL https://www.airbus.com/sites/g/files/jlcbta136/files/2023-10/Airbus_Defence_and_Space_Mechanisms_Products_2023.pdf. (Accessed 13 December 2023).

[132] General Dynamics, X-Band solid state power amplifier (SSPA), 2023, Online, URL https://gdmissionsystems.com/-/media/General-Dynamics/Space-and-Intelligence-Systems/PDF/spaceborne-x-band-sspa-datasheet.ashx?la=en&hash=9646562DB405E956EFCAC0D2A14AB7F9FB28983A. (Accessed 13 December 2023).

[133] General Dynamics, Small deep-space transponder (SDST), 2023, Online, URL https://gdmissionsystems.com/-/media/general-dynamics/space-and-intelligence-systems/pdf/small-deep-space-transponder-datasheet.ashx. (Accessed 13 December 2023).

[134] General Dynamics, S-band solid state power amplifier, 2023, Online, URL https://gdmissionsystems.com/-/media/general-dynamics/space-and-intelligence-systems/pdf/spaceborne-s-band-solid-state-power-amplifier-datasheet.ashx. (Accessed 13 December 2023).

[135] General Dynamics, Space qualified multi-mode standard transponder (MST) 400, 2023, Online, URL https://gdmissionsystems.com/-/media/general-dynamics/space-and-intelligence-systems/pdf/space-multi-mode-standard-transponder-mst-datasheet.ashx. (Accessed 13 December 2023).

[136] A.D. Pathak, S. Saha, V.K. Bharti, M.M. Gaikwad, C.S. Sharma, A review on battery technology for space application, J. Energy Storage (ISSN: 2352-152X) 61 (2023) 106792, http://dx.doi.org/10.1016/j.est.2023.106792, URL https://www.sciencedirect.com/science/article/pii/S2352152X23001895.

[137] T.W. Price, D.D. Evans, The status of monopropellant hydrazine technology, 1968, Online, URL https://ntrs.nasa.gov/api/citations/19680006875/downloads/19680006875.pdf. (Accessed 31 March 2025).

[138] J. Back, B. Schuettpelz, A. Ewing, G. Laue, James webb space telescope sunshield membrane assembly, in: 50th AIAA/ASME/ASCE/AHS/ASC Structures, Structural Dynamics, and Materials Conference, American Institute of Aeronautics and Astronautics, 2012, http://dx.doi.org/10.2514/6.2009-2156, URL https://arc.aiaa.org/doi/abs/10.2514/6.2009-2156.

[139] S. Nanthini, P. Veluswamy, H. Shankar, Protective coatings for high-temperature thermoelectric materials, in: Coatings for High-Temperature Environments: Anti-Corrosion and Anti-Wear Applications, Springer Nature Switzerland, Cham, ISBN: 978-3-031-45534-6, 2024, pp. 311–349, http://dx.doi.org/10.1007/978-3-031-45534-6_12.

[140] N.M. Jedrich, D.D. Zimbelman, W.L. Swift, F.X. Dolan, M.D. Brumfield, A mechanical cryogenic cooler for the hubble space telescope, in: Space Congress Proceedings, 2002, URL https://ntrs.nasa.gov/citations/20020070802.

[141] T. Maciaszek, A. Ealet, K. Jahnke, E. Prieto, R. Barbier, Y. Mellier, A. Costille, F. Ducret, C. Fabron, J.-L. Gimenez, R. Grange, L. Martin, C. Rossin, T. Pamplona, P. Vola, J.C. Clémens, G. Smadja, J. Amiaux, J.C. Barrière, M. Berthe, A. De Rosa, E. Franceschi, G. Morgante, M. Trifoglio, L. Valenziano, C. Bonoli, F. Bortoletto, M. D'Alessandro, L. Corcione, S. Ligori, B. Garilli, M. Riva, F. Grupp, C. Vogel, F. Hormuth, G. Seidel, S. Wachter, J.J. Diaz, F. Grañena, C. Padilla, R. Toledo, P.B. Lilje, B.G.B. Solheim, C. Toulouse-Aastrup, M. Andersen, W. Holmes, U. Israelsson, M. Seiffert, C. Weber, A. Waczynski, R.J. Laureijs, G. Racca, J.-C. Salvignol, P. Strada, Euclid near infrared spectrophotometer instrument concept and first test results at the end of phase b, in: J.M. Jr. Oschmann, M. Clampin, G.G. Fazio, H.A. MacEwen (Eds.), Space Telescopes and Instrumentation 2014: Optical, Infrared, and Millimeter Wave, in: Society of Photo-Optical Instrumentation Engineers (SPIE) Conference Series, vol. 9143, 2014, p. 91430K, http://dx.doi.org/10.1117/12.2056702.

[142] G.D. Racca, R. Laureijs, L. Stagnaro, J.-C. Salvignol, J. Lorenzo Alvarez, G. Saavedra Criado, L. Gaspar Venancio, A. Short, P. Strada, T. Bönke, C. Colombo, A. Calvi, E. Maiorano, O. Piersanti, S. Prezelus, P. Rosato, J. Pinel, H. Rozemeijer, V. Lesna, P. Musi, M. Sias, A. Anselmi, V. Cazaubiel, L. Vaillon, Y. Mellier, J. Amiaux, M. Berthé, M. Sauvage, R. Azzollini, M. Cropper, S. Pottinger, K. Jahnke, A. Ealet, T. Maciaszek, F. Pasian, A. Zacchei, R. Scaramella, J. Hoar, R. Kohley, R. Vavrek, A. Rudolph, M. Schmidt, The euclid mission design, in: H.A. MacEwen, G.G. Fazio, M. Lystrup, N. Batalha, N. Siegler, E.C. Tong (Eds.), Space Telescopes and Instrumentation 2016: Optical, Infrared, and Millimeter Wave, in: Society of Photo-Optical Instrumentation Engineers (SPIE) Conference Series, vol. 9904, 2016, p. 99040O, http://dx.doi.org/10.1117/12.2230762.

[143] W.L. Swift, F.X. Dolan, M.V. Zagarola, The nicmos cooling system—5 years of successful on-orbit operation, AIP Conf. Proc. (ISSN: 0094-243X) 985 (1) (2008) 799–806, http://dx.doi.org/10.1063/1.2908673.

[144] J.H. Henninger, Solar absorptance and thermal emittance of some common spacecraft thermal-control coatings, 1984, NTRS Author Affiliations: NASA Goddard Space Flight Center NTRS Report/Patent Number: REPT-84F0248 NTRS Document ID: 19840015630 NTRS Research Center: Legacy CDMS (CDMS), URL https://ntrs.nasa.gov/citations/19840015630.

[145] D.A. de Rooij, SPACEMATDB - space materials database, 2024, Online, URL https://www.spacematdb.com/spacemat/. (Accessed 10 June 2024).

[146] E. Lapeña, J. Herranz, F. Gómez-Carpintero, M. Rodríguez, The LEO PCDU EVO - a modular and flexible concept for low to medium power LEO & scientific missions, E3S Web Conf. 16 (2017) 18009, http://dx.doi.org/10.1051/e3sconf/20171618009.

[147] Saft, Saft solution for LEO and small GEO applications, 2023, Online, URL https://saft4u.saft.com/en/product/saft-solution-leo-and-small-geo-applications. (Accessed 13 December 2023).

[148] Azur Space, TJ solar cell assembly 3G30A, 2023, Online, URL https://www.azurspace.com/images/products/0003401-01-01_DB_3G30A.pdf. (Accessed 13 December 2023).

[149] Ariane Group, Ariane 6 user's manual for multi-launch service (MLS), 2021, Online, URL https://www.arianespace.com/wp-content/uploads/2021/07/MLSs-users-manual-ed0.0.pdf. (Accessed 13 September 2024).

[150] N. Rowlands, K. Smith, O. Daigle, O. Djazovski, A. Scott, A. Beaton, A. Wilson, Ultraviolet sensitivity of a teledyne-e2v EMCCD, in: A.D. Holland, J. Beletic (Eds.), in: High Energy, Optical, and Infrared Detectors for Astronomy VIII, vol. 10709, International Society for Optics and Photonics, SPIE, 2018, p. 107090D, http://dx.doi.org/10.1117/12.2313022.

[151] J.W. Beletic, J. Auyeung, J. Pan, L. Corrales, M. Dorn, D. Maitra, M. Farris, M. Zandian, E. Piquette, L. Rangel, A. Petersen, A. Yulius, Y. Bai, S. Bhargava, Teledyne imaging sensors' recent contributions to astronomy, earth science, and planetary science, Astron. Nachr. 344 (8–9) (2023) e20230136, http://dx.doi.org/10.1002/asna.20230136, URL https://onlinelibrary.wiley.com/doi/abs/10.1002/asna.20230136.

[152] A. Bayless, R. Rudy, L.J. Gelinas, J. Hecht, D.J. Gutierrez, K. Crawford, Pre-flight calibrations for the PIANO airglow camera on the ISS, in: Conference on Characterization and Radiometric Calibration for Remote Sensing, CALCON, 2021, URL https://digitalcommons.usu.edu/calcon/CALCON2021/all2021content/27/.

[153] P. Verhoeve, T. Prod'homme, T. Oosterbroek, N. Boudin, L. Duvet, CCD characterization for astronomy space missions at ESA, in: A.D. Holland, J. Beletic (Eds.), in: High Energy, Optical, and Infrared Detectors for Astronomy VI, vol. 9154, International Society for Optics and Photonics, SPIE, 2014, 915416, http://dx.doi.org/10.1117/12.2058110.